©2009 Society of Economic Geologists, Inc.
Economic Geology, v. 104, pp. 1143–1168

Development of Framboidal Pyrite During Diagenesis, Low-Grade Regional Metamorphism, and Hydrothermal Alteration*

ROBERT J. SCOTT[†,1], SEBASTIEN MEFFRE,[1] JON WOODHEAD,[2] SARAH E. GILBERT,[1] RON F. BERRY,[1] AND POUL EMSBO[3]

[1] *CODES, ARC Centre of Excellence in Ore Deposits, Private Bag 126, University of Tasmania, Australia 7001*

[2] *School of Earth Sciences, University of Melbourne, Australia 3010*

[3] *U.S. Geological Survey, Mail Stop 973, Denver, Colorado 80225*

Abstract

Distribution patterns, microstructural relationships, and compositional variations for framboidal pyrite in the Paleozoic sedimentary host rocks to gold deposits on the northern Carlin trend, Nevada, and at Fosterville in central Victoria, collectively demonstrate that it is not all of synsedimentary-early diagenetic origin. Framboidal pyrite also nucleated in hydrothermal veins formed at several kilometers depth and along dissolution surfaces (stylolites and crenulation cleavages) formed during metamorphism at up to anchizonal grade (i.e., prehnite-pumpellyite facies). There are no obvious differences in either the size range or internal morphology of framboids formed in these various settings, suggesting that a single, relatively simple crystallization path may operate over a wide depth range in the upper crust. At Fosterville, anomalously metal-rich (including Au) framboidal pyrite is most abundant adjacent to laminated shear veins that developed by slip along bedding surfaces during folding of the sedimentary host rocks. Microstructural relationships and Pb isotope compositions for the framboidal pyrite, and other similarly distributed, early-formed sulfides, support development in response to the localized, episodic influx of metal-enriched H_2S-bearing hydrothermal fluids during regional deformation between 440 and 400 Ma. These findings may have implications for other similarly deformed metasedimentary successions, where the discovery of Au-bearing framboidal pyrite has recently been cited as evidence for significant Au enrichment during sedimentation.

Introduction

FEW MINERAL textures have been the subject of such prolonged and detailed study as framboidal pyrite (e.g., Schneiderhöhn, 1923; Rust, 1935; Schouten, 1946; Love and Amstutz, 1966; Berner, 1970; Rickard, 1970, 1975; Sweeney and Kaplan, 1973; Raiswell, 1982; Morse and Cornwall, 1987; Wilkin et al., 1996, 1997; Wilkin and Barnes, 1997; Sawłowicz, 2000; Butler and Rickard, 2000; Ohfuji and Rickard, 2005; Ohfuji et al., 2005, 2006; Raiswell et al., 2008). Ohfuji and Rickard (2005) defined framboids as microscopic, spherical to subspherical clusters of equidimensional and equimorphic microcrystals. Individual pyrite framboids are generally 5 to 20 μm and rarely up to 250 μm in diameter. They typically contain 10^3 to 10^6 microcrystals, which are 0.1 to 20 μm in size but usually <2 μm in diameter (Love and Amstutz, 1966; Rickard, 1970; Wilkin et al., 1996; Sawłowicz, 2000; Ohfuji and Rickard, 2005). Microcrystals may be loosely packed and randomly oriented or densely packed and highly ordered, and pyrite can form anywhere between approximately 10 and 75 percent of the framboid volume (Rickard, 1970; Wilkin et al., 1996). X-ray and electron backscatter diffraction studies by Ohfuji et al. (2005, 2006) demonstrate that greater morphological ordering is reflected in greater uniformity in crystallographic orientation of the microcrystals.

Numerous studies of modern marine and nonmarine sediments demonstrate that framboidal pyrite forms readily, with production rates commonly at a maximum, within centimeters of the sediment-water interface, due to interaction between bacterially produced H_2S and detrital Fe minerals in the sediment (e.g., Love, 1967; Berner, 1970, 1984; Canfield et al., 1992; Wilkin et al., 1996; Raiswell and Canfield, 1998). In euxinic basins, where H_2S is present in the water column, framboidal pyrite may also form above the sediment-water interface (Raiswell and Berner, 1985; Skei, 1988; Wilkin et al., 1996, 1997). Framboidal pyrite is also associated with certain hydrothermal ore deposits, although many of these are known or interpreted to have formed at, or near, the sea floor (e.g., Rickard and Zweifel, 1975; Honnorez et al., 1976; Chen, 1978; England and Ostwald, 1993; Halbach et al., 1993; Pichler et al., 1999). Thus, while it is recognized that the formation of framboidal pyrite is not restricted to sedimentary environments, it is generally interpreted to be indicative of very shallow and relatively low temperature settings (e.g., <200°C, Rickard, 1970; Wilkin and Barnes, 1997).

To date, only a few studies provide examples of framboidal pyrite likely to have formed at significantly greater depth. Reedman et al. (1985) interpreted framboidal pyrite in quartz-pyrite-base metal veins from the Ordovician Snowdon Volcanic Group, North Wales to have formed at around 2-km depth. Framboidal pyrite in bitumen veins hosted by fractured lower Cretaceous rhyolite and andesite at the El Soldado Manto-type deposit in Chile is also interpreted to have formed at 2- to 3-km depth (Wilson and Zentilli, 1999; Wilson et al., 2003). Framboidal pyrite developed in, or spatially related to, hydrothermal veins has also been reported from Cambro-Ordovician shale at the Acton Vale quarry, Quebec (Sassano and Schrijver, 1989), Upper Ordovician black shale at Dolaucothi Gold Mine, Wales (Annels and Roberts, 1989), as well as in some Cornish tin deposits (Schouten, 1946).

Where framboidal pyrite is preferentially (or exclusively) developed in veins (e.g., Reedman et al., 1985; Sassano and

---

*A digital supplement to this paper is available at <http://www.geoscienceworld.org/> or, for subscribers, on the SEG website, <http://www.segweb.org>.

[†] Corresponding author: e-mail, robert.scott@utas.edu.au

Submitted: May 19, 2009
Accepted: November 2, 2009

Schrijver, 1989) or is intimately associated with other hydrothermal minerals (Honnorez et al., 1976; Chen, 1978; Pichler et al., 1999), direct precipitation from hydrothermal fluids appears likely. However, due to the limited mobility of Fe in many epigenetic mineralizing systems, pyrite is commonly best developed in hydrothermally altered originally Fe bearing rock adjacent to vein and fracture networks, rather than in the structures themselves. In such circumstances, the formation of epigenetic framboidal pyrite could easily go unrecognized, particularly in sedimentary rocks, which might reasonably be expected to contain framboidal pyrite of synsedimentary or early diagenetic origin. Indeed, the identification of anomalously metal-rich framboidal pyrite in the host successions to some sediment-hosted ore deposits has been cited as evidence that initial metal enrichment occurred during sedimentation or early diagenesis (e.g., Li et al., 1998; D.J. Large et al., 1999; Pitcairn et al., 2006; Large et al., 2007, 2009).

Here we report on the development of framboidal pyrite in the Paleozoic sedimentary rocks which host gold deposits on the northern Carlin trend, north-east Nevada, and in central Victoria, Australia. In both areas, pyrite distributions, overprinting criteria, and compositional data indicate that some framboidal pyrite must have formed tens to hundreds of millions of years after deposition of the host rocks, during (1) late diagenesis, (2) low grade metamorphism, and/or (3) hydrothermal alteration. Examples from central Victoria suggest that framboidal pyrite can form (in favorable microniches) at T-P conditions up to those of at least lower greenschist-facies metamorphism. Although framboid-size distributions were not quantified for this study (cf. Wilkin et al., 1996; Raiswell et al., 2008), framboids of early diagenetic and epigenetic origin are not obviously distinguished by differences in size or internal morphology. Thus in ancient rock sequences, additional data constraining the timing and distribution of framboidal pyrite should be sought (e.g., Annels and Roberts, 1989) before attaching genetic significance to either its occurrence or metal content.

Methods

Samples described here were collected as part of a larger study evaluating the evidence for syngenetic gold enrichment in the host sequences to major sediment-hosted epigenetic gold deposits (e.g., Large et al., 2007, 2009; Meffre et al., 2008; Scott et al., in prep.). Where aggregates of framboidal pyrite were large enough to be visible to the naked eye during core logging (pyrite morphology confirmed by subsequent microscopic examination), their stratigraphic context and/or spatial relationships to structural features (e.g., faults, veins, etc.) were noted. Subsequent analysis of framboidal pyrite distributions is based on microscopic examination of thin sections and polished blocks. Polished blocks were etched with cold 70 percent HNO_3 for 5 to 20 s in order to enhance internal textural features in the pyrite (e.g., Rickard and Zweifel, 1975).

Pyrite trace element compositions (summarized in Table 1, for complete data see electronic attachment) were determined by a laser ablation ICP-MS (LA-ICPMS), using sample preparation and analytical procedures described by Large et al. (2007) and Scott et al. (in prep.). Lead isotope compositions for paragenetically and microstructurally constrained pyrite and galena from Fosterville were determined by ICP-MS, using both the Agilent quadrupole ICP-MS at the University of Tasmania and the Nu Plasma multicollector ICP-MS (MC-ICPMS) at the University of Melbourne. Initial analyses were performed using the quadrupole instrument connected to a 213-nm solid-state laser, following procedures described by Meffre et al. (2008). Where possible, results were checked using the higher precision MC-ICPMS instrument following methods described in Woodhead et al. (2009).

To compensate for the lower analytical precision of the quadrupole ICP-MS, weighted averages for multiple analyses (typically 12) of texturally or microstructurally similar pyrite were determined using Ludwig's (2003) Isoplot software. Poor results were obtained for two samples in which aggregates of framboidal pyrite were partly filled in and/or replaced by galena. Poor data quality was due to large fluctuations in Pb count rates, which could not be maintained in the optimum range for the quadrupole instrument (i.e., 40,000–5,000,000 cps for ^{208}Pb, e.g., Meffre et al., 2008). The high Pb content of these samples precluded laser ablation analysis using the MC-ICPMS. However, galena from one of the samples (sample RHD019_161.56 m) was dissolved in a drop of concentrated HCl, after first cleaning the sample surface with double-distilled water. The acid was extracted by pipette and rinsed out with double-distilled water. The residue left after evaporation of the liquid was dissolved in 2 percent HNO_3 for analysis by solution ICPMS using the quadrupole instrument. The Pb isotope composition determined for the galena is the average of ten repeat analyses of the sample solution. Data were corrected for mass bias against a primary standard and galena from Que River, western Tasmania, analyzed by the same procedure, provided a secondary standard.

Framboidal Pyrite from the Northern Carlin Trend, Nevada

Framboidal pyrite is widely preserved in the Devonian sedimentary rocks that are the main hosts to gold deposits on the northern Carlin trend. Examples discussed here come from the upper Popovich and overlying Rodeo Creek Formations. Both units were deposited in outer carbonate shelf to basinal settings and consist of variably carbonaceous and pyritic, dolomitic, to locally siliceous siltstone and shale, with lesser interbedded calcarenite and lithoclastic to bioclastic debris flows (Armstrong et al., 1998; Furley, 2001; Scott et al., in prep.). During Early Mississippian emplacement of the now overlying Roberts Mountains allochthon, these strata passed through the oil generation window, and numerous hydrocarbon-filled veinlets (now pyrobitumen or graphite) formed in and adjacent to originally organic-rich rocks (Kuehn and Rose, 1992; Emsbo and Koenig, 2007). These veinlets are particularly useful to pyrite paragenetic studies, as crosscutting relationships provide a basis for discriminating early diagenetic pyrite (i.e., prehydrocarbon generation) and later diagenetic and/or hydrothermal pyrite (Scott et al., in prep.).

Framboidal pyrite of interpreted early diagenetic origin

Framboidal pyrite of interpreted synsedimentary to early diagenetic origin occurs throughout the Popovich and Rodeo Creek Formations, however, it is best developed in the Soft-Sediment Deformation unit and basal part of the overlying

TABLE 1. Selected LA-ICPMS Trace Element Data (ppm)

Analysis	Type[1]	Al	V	Co	Ni	Cu	As	Se	Mo	Ag	Sb	Au	Tl	Pb	Th	U
CD12c (852.6 ft), Goldstrike, northern Carlin trend																
FE05A40	Pre-bitumen vein	3357	49	2	492	147	307	180	271	2.6	74	<0.92	3.4	68	0.78	2.48
FE05A55	Post-bitumen vein	6652	95	224	4482	3499	1062	143	961	45.6	588	<0.92	127.3	656	1.31	8.23
QRC1750 (22 ft), Gold Quarry, northern Carlin trend																
OC09A09a	Outer colloform mc/py	14	1	<2	13	<15	116514	<43	40	<2.2	4578	<0.50	244.9	20	<0.27	<0.25
OC09A09b	Inner colloform mc/py	10	9	<2	32	17	88870	<43	42	<2.2	6066	<0.50	1089.1	14	<0.27	<0.25
OC09A09c	Framboid dominant	12	4	<2	200	27	29541	<43	<19	<2.2	6233	2.13	1712.4	14	<0.27	<0.25
GT8 (23.2 m), Fosterville																
JA11A36	Pre-S_2 py nodule (outer)	4147	6	68	359	107	3599	37	261	0.5	89	0.03	18.6	275	1.51	0.83
JA11A37	Pre-S_2 py nodule (inner)	1753	3	2	54	42	301	5	61	0.7	40	0.03	3.1	95	0.52	0.30
JA11A47	Pre-S_2 cluster f.g. py	1656	2	54	183	182	171	<17	4	3.1	159	0.15	0.6	426	0.17	0.04
GT8 (49.4 m), Fosterville																
JN28A92	Pre-S_2 fram aggregate	10989	10	1686	553	1174	3107	26	112	20.4	592	1.72	0.7	6069	<0.06	0.15
JN28A92	Pre-S_2 fram aggregate	10989	10	1686	553	1174	3107	26	112	20.4	592	1.72	0.7	6069	<0.06	0.15
GT8 (94.4 m), Fosterville																
JN28A107	Pre-S_2? fram	69883	196	1012	1017	629	1951	<24	<12	4.0	444	<0.65	4.9	375	3.92	6.57
JN28A109	Pre-S_2? isolated py euhedra	77	<1	1490	395	401	1146	<66	29	17.5	284	<0.59	1.5	758	<0.19	<0.18
JN28A115	Pre-S_2 f.g. py / mc	154	<1	903	458	1025	1700	26	258	13.6	211	1.56	2.7	484	<0.10	<0.1
DALD017 (66.28 m), Daly's Hill area, Fosterville																
NO08A04	Pre-S_2 cluster f.g. py	524	1	38	556	138	1191	16	110	5.0	223	1.14	21.4	216	0.04	0.08
NO08A10	Pre-S_2 py nodule core	186	1	1	62	31	4069	<3	73	1.0	187	0.27	17.2	78	<0.02	<0.02
SPD213 (391.90 m), Fosterville																
JL11A64	Pre-/syn-S_2 fram and o'growth	3214	27	1012	818	1435	7353	96	244	25.5	651	1.37	52.8	2315	0.13	0.37
JL11A65	Pre-/syn-S_2 fram in matrix	152033	1234	1105	1869	1930	3923	142	266	30.6	955	1.31	32.8	2316	126.25	24.59
JL11A66	Pre-/syn-S_2 py o'growth	976	9	660	345	240	4044	106	215	9.7	239	<0.86	16.8	316	0.14	0.28
RHD019 (161.56 m), O'Dwyers pit area, Fosterville																
MY11A11	Pre-/early syn-S_2 f.g. py	2321	24	72	613	56	1169	<40	<13	<2.1	46	1.22	<0.2	136	4.30	8.35
MY11A17	Pre-/early syn-S_2 gal incl. in cpy	<4	<1	<1	<6	12746	<45	19253	<13	96.3	202	<0.45	3.1	866000	0.80	0.38
MY11A18	Pre-/early syn-S_2 framb and f.g. euh py	177	2	396	4047	1434	1809	200	<13	2.8	31	1.22	<0.2	13101	2.76	8.68
RHD019 (161.42 m) , O'Dwyers pit area, Fosterville																
JN28A88	Syn-S_2 fram	153871	799	3505	2041	1899	3455	<45	<30	9.5	1199	13.99	20.0	3360	8.73	8.56
JN28A90	Syn-/post-S_2 py euhedra	2202	11	568	949	60	1466	<20	10	2.5	213	2.35	1.8	825	0.99	0.38

[1] Abbreviations used in table: cpy = chalcopyrite, f.g. = fine-grained (for pyrite, typically mixtures of framboidal or framboidlike microcryst aggregates, interspersed with or overgrown by fine-grained euhedral pyrite), fram = framboidal pyrite, gal = galena, mc = marcasite, o'growth = overgrowth, py = pyrite, sph = sphalerite

Upper Mud unit of the Popovich Formation, where it is locally the dominant pyrite type (abundances <2–3 percent, Scott et al., in prep.). It has several common modes of occurrence: (1) sparsely disseminated through the sediment matrix, (2) irregular-shaped and spheroidal polyframboidal clusters (e.g., Love, 1971) clusters, and (3) as minor to major constituents of bedding-parallel lenticular aggregates and laminae of other very fine grained pyrite (Fig. 1). Commonly, all types occur in a single sample. Lenticular aggregates are locally cut by Mississippian bitumen veinlets and are commonly overprinted by soft-sediment slump and compaction features (Fig. 1A), the latter indicating probable formation within

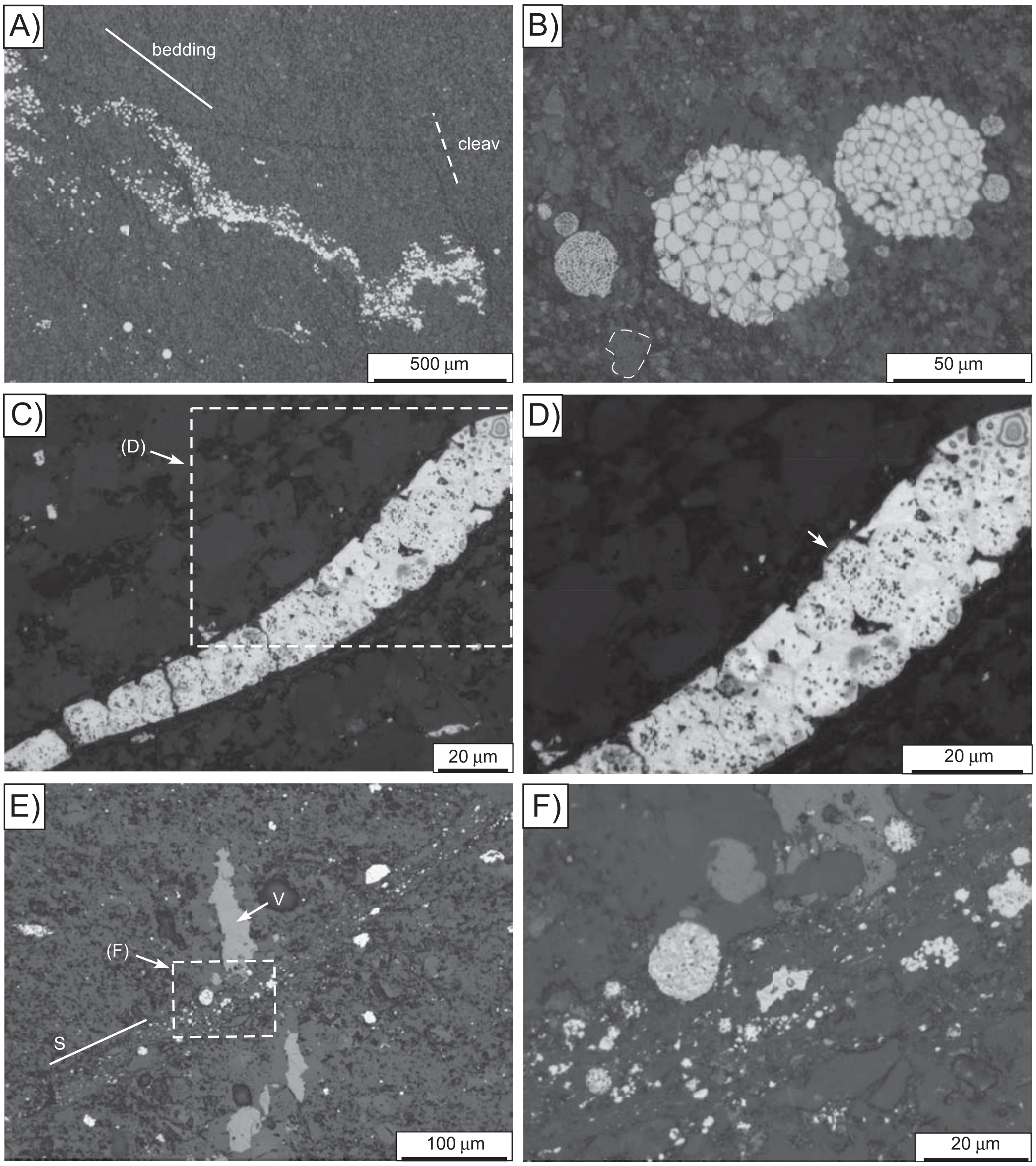

FIG. 1. Reflected-light photomicrographs of early and late diagenetic framboidal pyrite from the northern Carlin trend, Nevada. A. Bedding-parallel aggregates of very early diagenetic framboidal pyrite overprinted by soft-sediment slump folds and Mississippian(?)-age cleavage. Devonian Popovich Formation, drill hole BSC168c, 853 ft. B. Variation in size and internal morphology of pyrite framboids from same sample as (A). Some framboids are considerably larger than the largest detrital grains (e.g., dashed line at lower left). Note larger framboids have rims and infill of later pyrite. C. Small bioclast almost completely replaced by framboidal pyrite. Basal Upper Mud unit of the Popovich Formation, drill hole GA54c, 1484 ft. D. Detail from (C). Note that the surfaces of the outermost framboids conform to the original shape of the bioclast. E. Framboidal and other fine-grained pyrite concentrated along a late diagenetic stylolitic dissolution seam (S) that cuts a Mississippian bitumen veinlet (V). Rodeo Creek Formation, drill hole CD12c, 852.6 ft. F. Detail from (E).

meters of the sediment-water interface (e.g., Emsbo et al., 1999; Scott et al., in prep.).

Particularly in samples where framboidal pyrite is relatively abundant, there is considerable variation in both the size and internal morphology of the framboids (Fig. 1B). The largest framboids are commonly many times larger than the grain size of the host sediment (Fig. 1B), indicating they did not form in interstitial pore spaces, as assumed in many models of framboid precipitation. Aggregates of framboidal pyrite also replace organic matter and fossil fragments (Fig. 1C, D), and in such cases, the external morphology of the outermost framboids may conform to the original shape of the replaced fragment. There is commonly partial infilling by later pyrite (Fig. 1B) and/or other sulfides (e.g., sphalerite) of both individual framboids and spheroidal polyframboidal clusters.

Framboidal pyrite of interpreted late diagenetic origin

Very fine grained and framboidal pyrite is also concentrated along stylolitic seams that cut both early bedding-parallel pyrite aggregates and Mississippian bitumen veinlets (Fig. 1E, F). The stylolitic seams developed both parallel and oblique to bedding and may have formed during emplacement of the Roberts Mountains allochthon, continued burial, or later (e.g., Mesozoic) deformation events. Significant differences in the composition (Fig. 2, Table 1) and morphology of pyrite in the stylolites, compared to early-formed pyrite in the surrounding rock, suggest that pyrite enrichment along stylolites is not (primarily) due to the concentration of existing, relatively insoluble phases during stylolite development. However, determining the trace element compositions of fine-grained pyrite is potentially problematic in cases such as this, where analytical volumes exceed the pyrite grain size. Trace elements from the surrounding matrix and inclusions of other phases may contribute significantly to the apparent composition of fine-grained pyrite (Raiswell and Plant, 1980) and in particular framboidal pyrite, where 25 to 90 percent of the framboid volume is composed of material other than pyrite (e.g., Rickard, 1970; Love et al., 1984). Nonetheless, whether or not specific trace elements occur principally in pyrite can be assessed from their correlation with elements that do not occur at significant concentration in pyrite but do in minerals comprising the surrounding matrix (e.g., Al, Si, Mg, and Ca; e.g., Raiswell and Plant, 1980).

The laser ablation ICP-MS analyses of framboidal pyrite in sample CD12c_852.6 ft (e.g., Fig. 3) indicate that variations in the abundance of Pb, Cu, Sb, Co, Mn, Mo, As, Tl, Zn, Ag, and Se generally correlate moderately to strongly with Fe and poorly with Al (phyllosilicates), Mg-Ca (dolomite), and Si (quartz and phyllosilicates). This indicates these elements are either predominantly contained in pyrite or occur in phase(s) that are spatially related, and in constant proportion, to pyrite. Vanadium, on the other hand, is strongly correlated with Al, suggesting it principally resides in clay or mica (Fig. 2A). Thus, apparently higher V concentrations for the stylolite-hosted pyrite simply reflect higher proportions of matrix in these analyses, compared to those for the denser bedding-parallel pyrite aggregates.

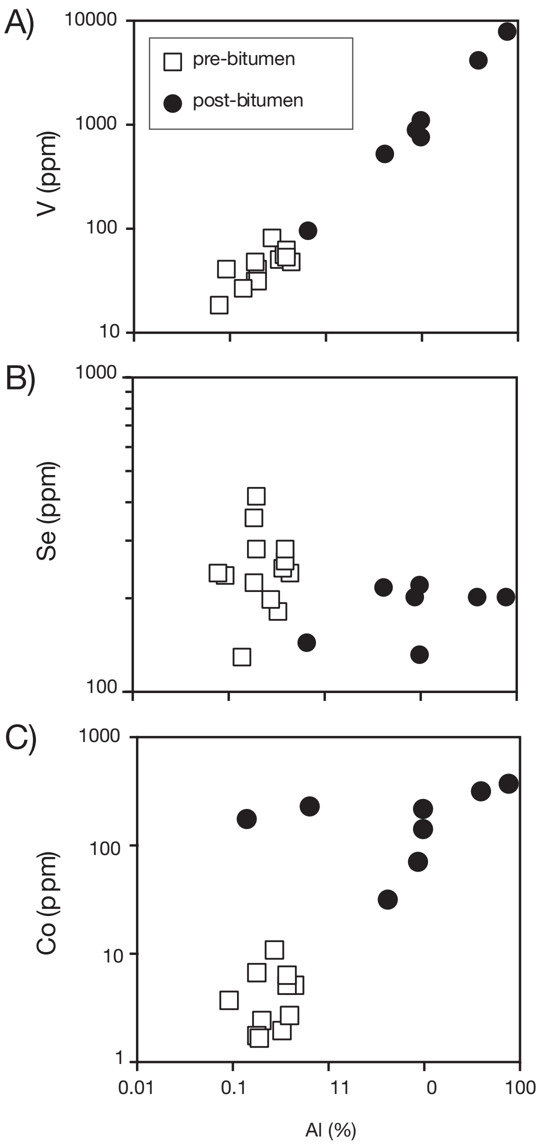

FIG. 2. Scatter plots showing variations in abundance of (A) V, (B) Se, and (C) Co relative to Al in LA-ICPMS data for early and late diagenetic pyrite from sample CD12c_852.6 ft. (see Fig. 1E, F). Data are quantified assuming all elements are contained in pyrite. For elements primarily contained in other minerals (e.g., inclusions or surrounding matrix), only element ratios are likely to be meaningful. Strong correlation between V and Al suggests the apparently higher V content of pyrite in the stylolites reflects a higher proportion of V-bearing clay or mica in these analyses. Variations in Se and Co are independent of Al and interpreted to reflect differences in pyrite composition.

Framboidal pyrite of interpreted late hydrothermal origin

Framboidal pyrite also occurs in some late Carlin ore-stage (i.e., Eocene) pyrite-marcasite veins (Fig. 4). Unlike Carlin ore-stage pyrite, which is all extremely fine grained (mostly <1 μm) and primarily developed in the wall rocks with Fe sourced from dissolution of adjacent Fe-bearing minerals (Cline et al., 2005), late ore-stage mineralization displayed greater Fe mobility with the local development of micro-colloform-textured pyrite and/or marcasite veins (Emsbo et al., 2003). Pyrite and/or marcasite precipitated in the late-stage veins is compositionally distinctive, being strongly enriched in As, Sb, and Tl but with lower to much lower levels of the other trace elements generally contained in ore-stage Carlin-type pyrite (e.g., Au, Ag, Cu, Pb; Emsbo et al., 2003).

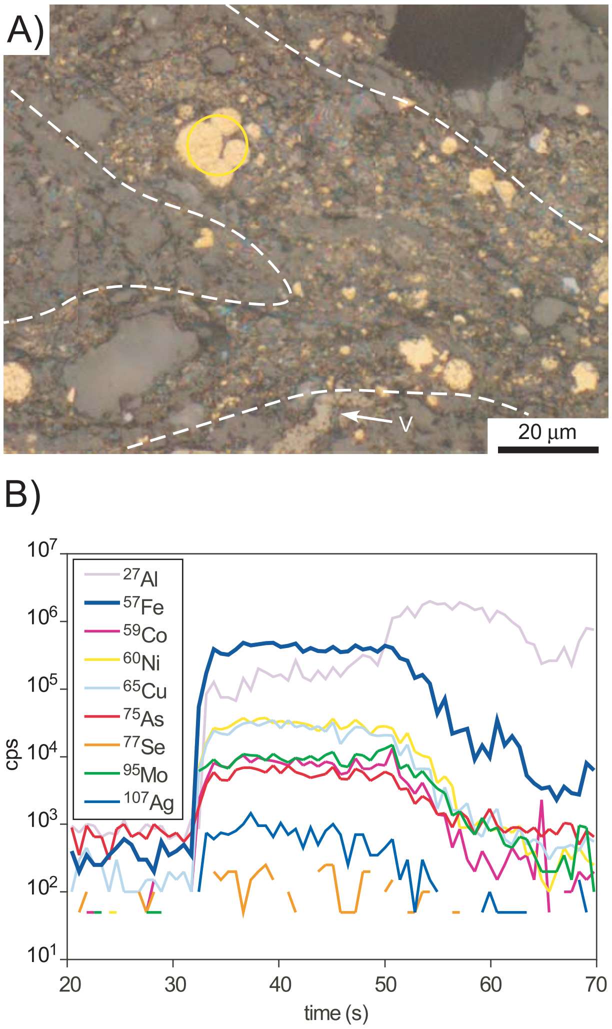

FIG. 3. A. Framboidal and fine-grained pyrite in stylolites (delineated by white dashed lines) truncating a Mississippian bitumen veinlet (V), Rodeo Creek Formation, drill hole CD12c, 852.6 ft. Yellow circle denotes location of LA-ICPMS analysis shown in (B). B. Plot showing variations in count-rate for selected trace elements during analysis of the small framboidal pyrite cluster shown in (A). The laser was turned on at 32 s and burned through the framboid cluster after 20 s (reflected by an abrupt decrease in signal for Fe and increase for Al). Variations in count-rate (proportional to abundance) for the other elements shown reflect proportion of Fe, rather than elements concentrated in the surrounding matrix (e.g., Al). See text for further discussion.

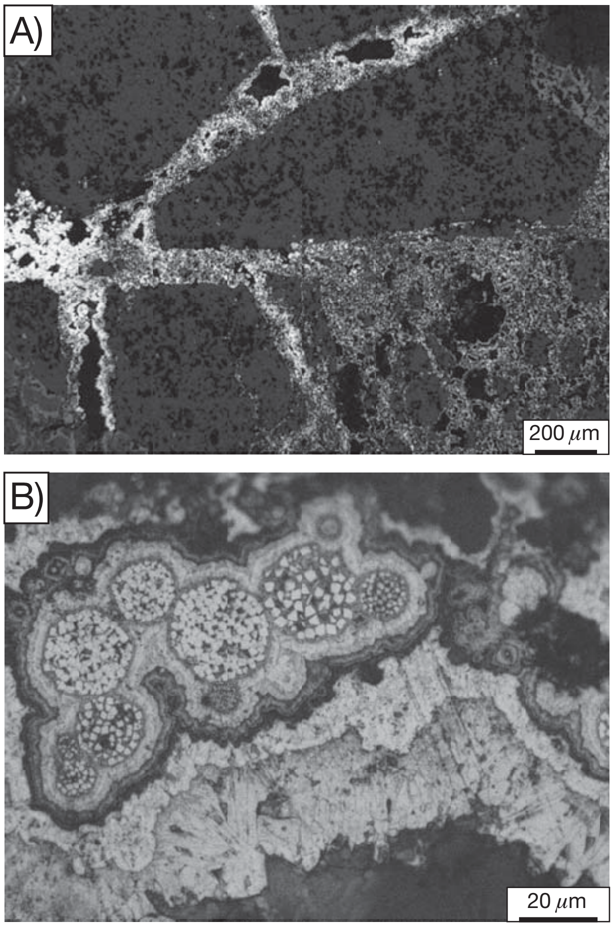

FIG. 4. Reflected-light photomicrographs of polished and acid-etched sample of late Carlin ore-stage marcasite veins and breccia fill, drill hole QRC1750, 22 ft, Rodeo Creek Formation, Gold Quarry mine. A. Veins consist principally of microcolloform banded marcasite. No framboidal pyrite is present in the wall rocks beyond the limits of intense sulfidation (e.g., lower left). B. Close-up showing framboids rimmed by the earliest marcasite growth stage.

Homogenization temperatures for fluid inclusions in quartz from late ore-stage veins have a mean of 220°C and a minimum of 175°C (Lamb, 1995; Emsbo et al., 2003). Most Carlin-type deposits are interpreted to have formed between 1- and 3-km depth (Cline et al., 2005), and a similar depth range for the late Carlin ore-stage veins is likely. Isotopic and compositional characteristics suggest that late ore-stage fluids formed by mixing between the Carlin ore fluid and cooler, more oxidized meteoric water during the waning stages of the hydrothermal system (Emsbo et al., 2003).

Laser ablation ICP-MS analyses indicate that both framboids and colloform-textured marcasite in a late ore-stage vein from the Gold Quarry mine (sample QRC1750_22 ft, Fig. 4, Table 1) are highly enriched in arsenic (2.9–12.0%), antimony (0.4–1.9%), and thallium (176–4,280 ppm). While the spatial resolution of the laser does not permit clear compositional discrimination of the framboids and the enveloping marcasite, analyses cenetred on framboids suggest these are preferentially slightly enriched in gold (i.e., 0.5–1.5 ppm Au), consistent with the interpreted late Carlin ore-stage timing (e.g., Emsbo et al., 2003). Framboidal pyrite in sample QRC1750_22 ft is restricted to veins or immediately adjacent halos of intensely sulfidized wall rock and is always overgrown by the earliest stage of microcolloform textured marcasite (Fig. 4B). The framboids exhibit the same range in size and microcrystal shape, size, and packing arrangement as those interpreted to be of early diagenetic origin (cf. Figs. 1B, 4B).

Framboidal Pyrite from Lower Paleozoic Turbidites, Fosterville, Central Victoria

Framboidal pyrite is minor (<<1%) but widespread in the tightly folded Lancefieldian (i.e., lowermost Ordovician) deep marine turbidites that host the >3 Moz Au (Hitchman et al., 2008) Fosterville gold deposit, central Victoria, Australia (Fig.

5). The succession is part of the Lower to Middle Ordovician Castlemaine Group, which hosts numerous small to large gold deposits in the Bendigo zone (Fig. 5A). Most deposits in this region formed at ca. 440 Ma, during the waning stages of fold and cleavage development in the Late Ordovician–Early Silurian Benambran orogeny (Arne et al., 1998; Foster et al., 1998; Willman, 2007), and contain predominantly fault- and vein-hosted free gold (Cox et al., 1995; Schaubs and Wilson, 2002). In contrast, the Fosterville deposits (1) are Devonian (e.g., mineralized felsic dikes with zircon U-Pb ages ranging

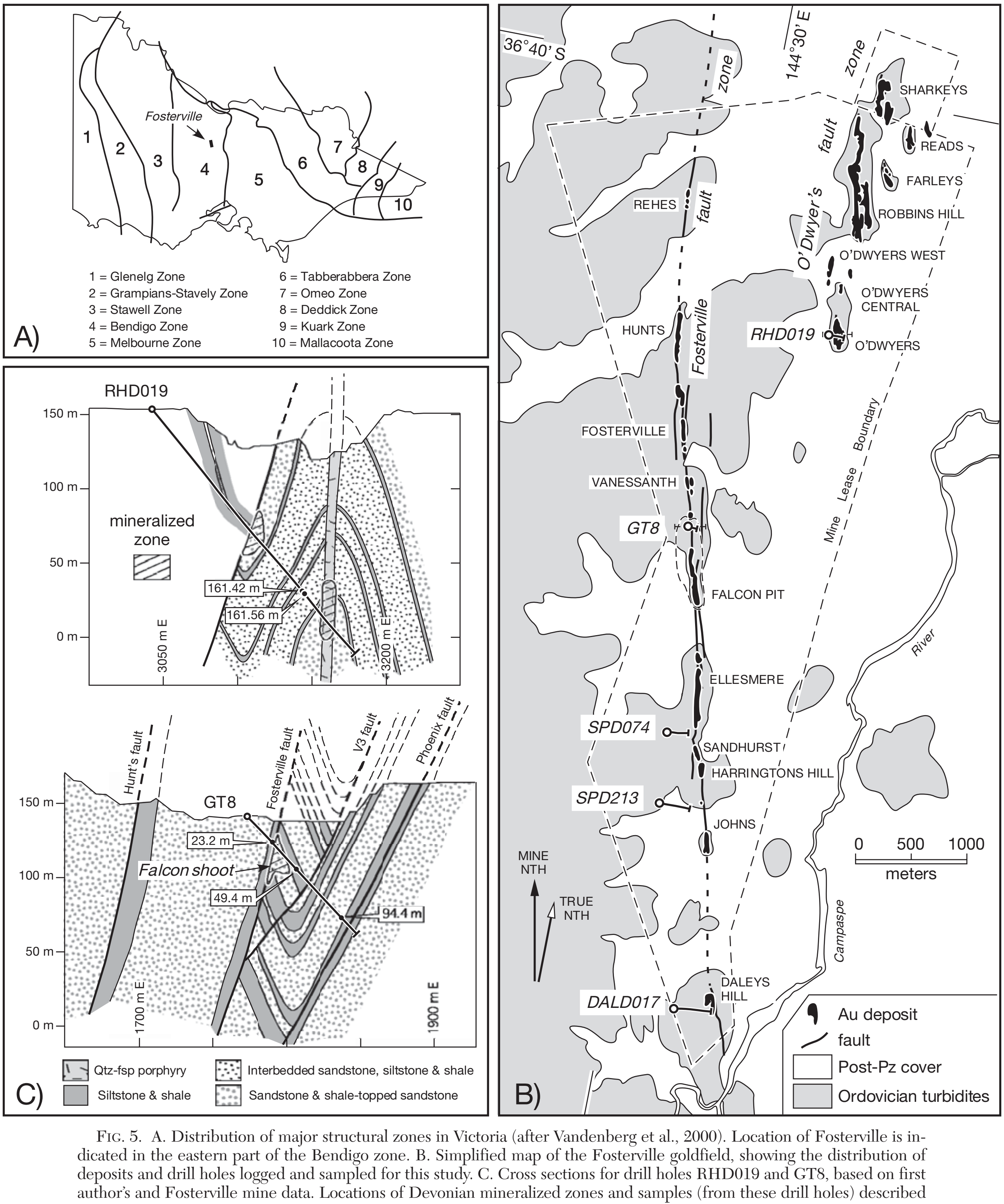

FIG. 5. A. Distribution of major structural zones in Victoria (after Vandenberg et al., 2000). Location of Fosterville is indicated in the eastern part of the Bendigo zone. B. Simplified map of the Fosterville goldfield, showing the distribution of deposits and drill holes logged and sampled for this study. C. Cross sections for drill holes RHD019 and GT8, based on first author's and Fosterville mine data. Locations of Devonian mineralized zones and samples (from these drill holes) described in this study are indicated.

from 394 ± 17 to 371 ± 6 Ma: Arne et al., 1998; Bierlein et al., 2001a), (2) formed during reverse-sinistral reactivation of the earlier Fosterville and O'Dwyers fault zones (Fig. 5; Wang and White, 1993; Leader et al., 2010), and (3) contain refractory gold in disseminated, wall-rock–hosted fine-grained arsenopryite and arsenian pyrite; Zurkic, 1998; Mernagh, 2001; Bierlein et al., 2000, 2004). The host rocks at Fosterville were metamorphosed to anchizonal grade (prehnite-pumpellyite facies) during the Benambran orogeny and progressively exhumed during the Devonian (Offler et al., 1998).

Framboidal pyrite distribution at Fosterville

Framboidal pyrite is rare in the ore zones at Fosterville but ubiquitous in surrounding shales and siltstones. However, it only occurs in high enough concentrations to be visible to the naked eye in the wall rocks adjacent to laminated, bedding-parallel, quartz-carbonate shear veins (Fig. 6) and locally in wall-rock fragments in the veins themselves. Here framboidal pyrite is generally associated with disseminated or nodular aggregates (Fig. 6A, C) of coarser grained subhedral to euhedral pyrite (and rarely, marcasite) and locally trace amounts of fine-grained chalcopyrite, sphalerite, and galena. Sulfide contents rarely exceed a few percent and decrease abruptly within a few, to a few tens of centimeters of the veins. Rarely, pyrite nodules and bedding-parallel bands of fine-grained and framboidal pyrite occur up to several meters from the veins. Based on morphology, much of this pyrite has previously been interpreted as sedimentary or diagenetic in origin (e.g., Bierlein et al., 2004) and some clearly predates development of the axial planar cleavage (e.g., Figs. 6, 7). However, the apparent restriction of significant sulfide development to either major fault zones (e.g., Fosterville fault, Fig. 5B, C) or the wall rocks within several meters of bedding-parallel shear veins (Fig. 6), suggests it formed during later, structurally controlled hydrothermal fluid flow.

Laminated bedding-parallel shear veins are common features of the Castlemaine Group and interpreted to have formed during folding as a result of localized flexural slip in thick incompetent beds or at interfaces between beds of different rheology (Jessell et al., 1994; Fowler, 1996; Fowler and Windsor, 1997). Larger veins generally occur in thicker shale, slate, or siltstone units, commonly within 10 cm of overlying sandstone beds (Jessell et al., 1994; Cox et al., 1995; Fowler, 1996; Boucher et al., 2008). Stratigraphic separation of the bedding-parallel veins at Fosterville ranges from 1 to 20 m, and is similar to other goldfields in the Bendigo zone (e.g., Jessell et al., 1994; Fowler and Windsor, 1997).

Many of the veins continue around fold hinges without significant changes in thickness, suggesting they formed early during folding (Willman and Wilkinson, 1992; Jessell et al., 1994; Willman, 2007); however, most clearly postdate initial axial planar cleavage development (Fowler, 1996). At Fosterville, overprinting relationships indicate that major

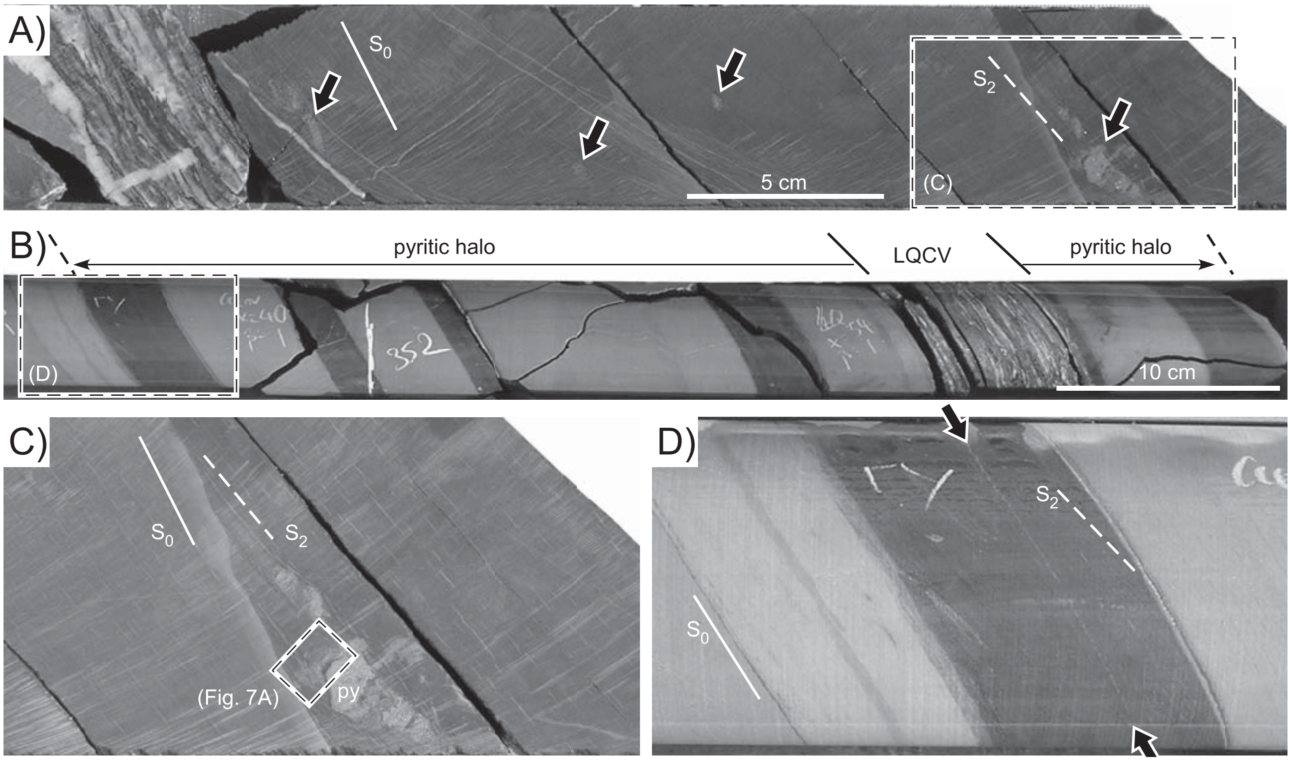

Fig. 6. Sulfide development adjacent to bedding-parallel laminated veins at Fosterville. A. Small nodules of fine-grained anhedral to euhedral pyrite (indicated by arrows) in siltstone and shale in the footwall of a narrow laminated vein (left). Area shown in (C) outlined by dashed box. Fosterville drill hole DALD017, 66.28 m. B. 5-cm-wide laminated quartz-carbonate shear vein (LQCV) in variably carbonaceous, sericite-carbonate altered shale and siltstone. Halo of visible sulfide development and area pictured in (D) are indicated. Fosterville drill hole SPD213, 351.90 m. C. Close-up of pyrite nodule from (A). Area of Figure 7A is outlined by dashed box. D. Close-up of carbonaceous bed (illustrated in (B)) containing a 3-mm-wide, bedding-parallel band of densely clustered framboidal pyrite (between arrows).

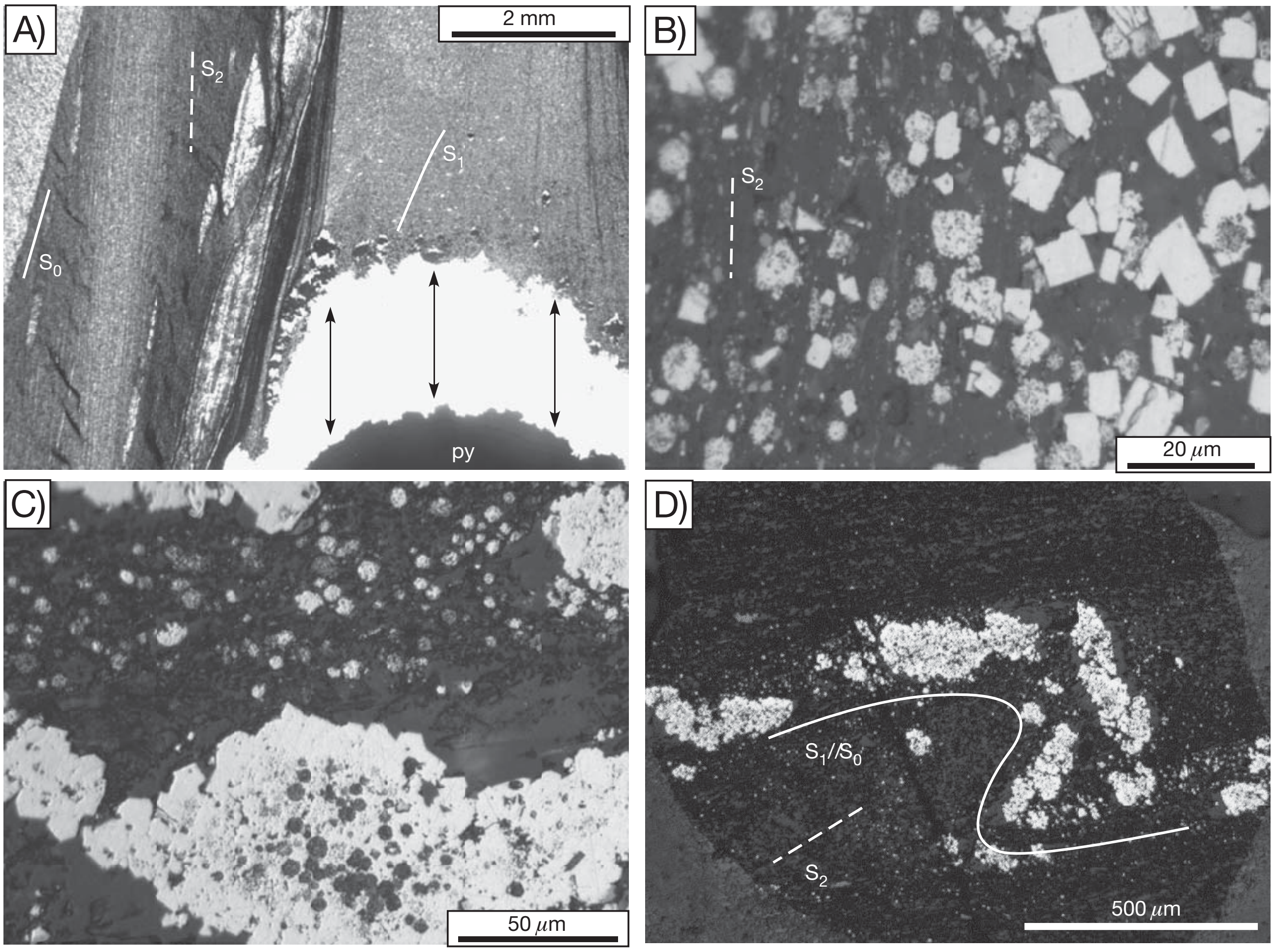

FIG. 7. Plane-polarized (A) and reflected (B–D) photomicrographs showing overprinting and textural relationships for pyrite formed early during or prior to S_2. A. Heterogeneous cleavage development in shale around the pyrite nodule illustrated in Figure 6C. Except where overprinted by S_2, there is little variation in either the intensity or orientation S_1 around the margins of the nodule, whereas S_2 does not occur in well-developed D_2 strain shadows at either end of the nodule. Fibrous quartz (white) in strain fringes records S_2 parallel extension. B. Framboidal pyrite concentrated around the margins of the nodule illustrated in Figure 6C is partially overgrown (±replaced) by coarser grained euhedral pyrite that makes up the bulk of the nodule. C. Coarser grained euhedral pyrite overgrowths on framboidal pyrite aggregates making up the pyritic band illustrated in Figure 6D. D. F_2 microfolds overprint both the framboid-rich band and later nodular pyrite overgrowths illustrated in Figures 6D and 7C.

movement on the veins predated Devonian gold mineralization (Wang and White, 1993), and many (particularly in the hanging wall of the Fosterville fault zone) were not obviously reactivated during that event.

Sulfide paragenesis and microstructural relationships

All but one of the samples discussed here are from positions <2 m (distances measured perpendicular to bedding) from bedding-parallel shear veins. Four main spatial and/or microstructural associations of framboidal pyrite are recognized: (1) minor, scattered individual framboids in shales, siltstones, and some sandstones; (2) concentrations around and overgrown by pyrite nodules; (3) discontinuous trails and elongate aggregates parallel to bedding and a cryptic, fine-grained mica foliation (S_1); and (4) concentrations along the axial planar cleavage (S_2). Framboids of association (1) are generally of ambiguous or indeterminate timing and are mostly too small (<<10 μm diam) and sparsely disseminated to be meaningfully analyzed by LA-ICPMS. As a result they are not considered further here.

Pre- to early syncleavage framboidal pyrite: Framboidal pyrite is concentrated around the margins of many dense (nodular) aggregates of fine-grained anhedral to euhedral pyrite. Nodules primarily occur in shales and silty shales, generally within 1 m of bedding-parallel shear veins (Fig. 6A, C). They are irregular to ovoid in shape and up to 3 cm in maximum dimension. Commonly at their peripheries (and less commonly through their interiors) well-preserved framboids are evident in the cores of some euhedral pyrite grains (Fig. 7B), indicating the coarser grained largely postdates the framboidal pyrite (e.g., Rickard and Zweifel, 1975; Raiswell and Plant, 1980). The extent to which framboidal pyrite also recrystallized to form the later pyrite (e.g., Large et al., 2007) is not clear.

Well-developed quartz-filled strain fringes and variations in both the intensity and orientation of S_2 around the nodule margins indicate that most formed very early during or before development of the axial planar cleavage (Fig. 7A). In contrast (although partly obscured by S_2), the cryptic, fine-grained, bedding-parallel mica foliation (S_1), which appears to represent the main episode of metamorphic mica growth in these rocks, is generally of similar intensity and orientation around the nodules, suggesting they may overgrow this fabric.

Most framboidal pyrite at Fosterville occurs in thin, discontinuous trails or elongate densely clustered aggregates aligned parallel to bedding and S_1 (i.e., association (3) above). In the best developed example (sample SPD213_351.90 m), a 3-mm-wide bedding-parallel band of densely clustered framboidal pyrite spans the entire 4.7-cm width of the drill core (Fig. 6B, D). This band occurs at the outer margin of a 30-cm halo of fine-grained disseminated sulfides developed in the hanging wall of a 7-cm-wide laminated bedding-parallel shear vein (Fig. 6B). More commonly, however, framboid aggregates are up to several millimeters long and <200 μm wide (Fig. 8) or form spheroidal clusters up to 200 μm in diameter. Some are mixtures of true framboidal pyrite (e.g., Ohfuji and Rickard, 2005) and irregular clusters of pyrite microcrystals. Overgrowths of later, coarser grained pyrite are relatively common (Figs. 7C, 9B-D), with some partial framboid cluster infilling or replacement by chalcopyrite, sphalerite, and galena (Figs. 8, 9B, C).

The S_1 parallel framboidal pyrite aggregates (and commonly overgrowths of coarser grained pyrite) are overprinted by S_2, indicating they formed during or prior to the earliest stages of cleavage development. Their timing with respect to S_1 is more equivocal. Many framboid aggregates have small quartz- or mica-filled strain fringes recording S_2 parallel extension along their edges (Fig. 8A) but no similar features recording S_1 parallel extension have been observed, even where S_1 is strongly developed.

Syn- to postcleavage framboidal pyrite: Abundant pyrite framboids, <10 μm in diameter, occur in a discontinuous thin band along the hanging-wall contact of a reactivated bedding-parallel quartz-carbonate vein in sample RHD019_161.42 (i.e., dark material indicated by white arrow in Fig. 9A). The framboidal pyrite principally occurs in domains of well-developed S_2 and is largely absent from the intervening microlithons (Fig. 9E, F). This distribution suggests the framboids mostly formed during or after S_2. Furthermore, numerous ovoid to lenticular aggregates of pyrite microcrystals within the S_2 domains are aligned parallel to the cleavage (Fig. 9G). The size, shape, and orientation of these aggregates suggest they may be flattened, originally spherical framboids. If so, differences in the amount of flattening may indicate protracted framboid nucleation during cleavage development.

In sample GT8_94.4 m (see Fig. 5C for location), sulfide distributions and overprinting relationships suggest that both pre- (to early syn-) S_2 and late syn-S_2 framboidal pyrite occur in a 1.5-cm-thick shale layer containing very thin, bedding-parallel shear vein (Figs. 10, 11). Most of the framboidal pyrite occurs in thin, relatively continuous, bedding and/or S_1 parallel bands and laminae that are clearly offset by S_2 (Fig. 11). Denser clusters are typically overgrown by coarser grained euhedral pyrite (and lesser marcasite) that also largely predates the cleavage. However, framboidal pyrite that is less commonly overgrown by euhedral pyrite is also concentrated along S_2 (Figs. 10C-D, 11). This could be due to concentration of existing, relatively insoluble minerals along cleavage domains (e.g., Gray, 1979; Gray and Durney, 1979), however later sulfide development along S_2 is also suggested by the apparent restriction of minute galena grains to these domains (Fig. 10C), as well as a slight increase in the grain size of S_1 parallel pyrite lamellae where reoriented along S_2 (Fig. 11).

Volume loss from S_2 cleavage domains at Fosterville

Previous studies in the central Victorian goldfields indicate that Ti was essentially immobile during deformation and hydrothermal alteration (e.g., Glasson and Keays, 1978; Gao and Kwak, 1997). Thus to determine whether pyrite concentrations along S_2 in sample GT8_94.4 m reflect the concentration of relatively insoluble phases by dissolution, volume loss from the cleavage domains was estimated by comparing their Ti contents to those of the adjacent microlithons. Element variations along eight adjacent LA-ICPMS line analyses for a 240- × 500-μm area of relatively low pyrite density in

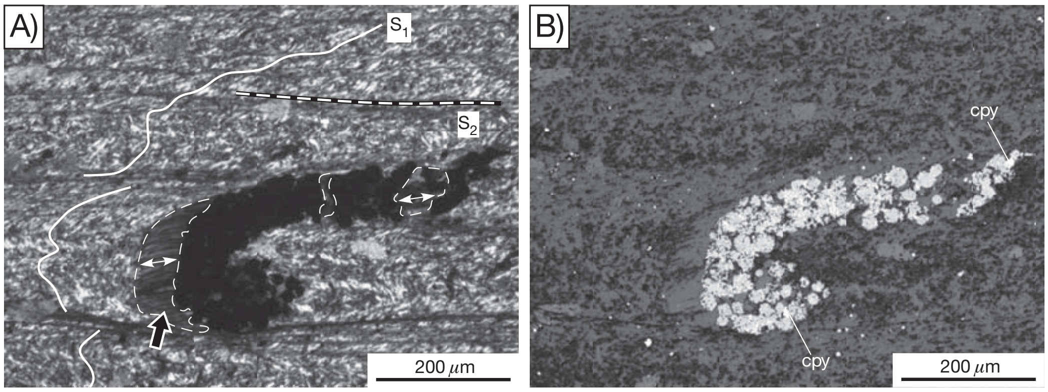

FIG. 8. (A) Cross-polarized light, and (B) reflected-light photomicrographs of an S_1 parallel lenticular aggregate of framboidal pyrite from Fosterville (sample GT8_49.4 m, see Fig. 5C for location). The aggregate is folded by S_2, partly filled by chalcopyrite (cpy), and has small strain fringes (outlined in A) recording S_2 parallel extension.

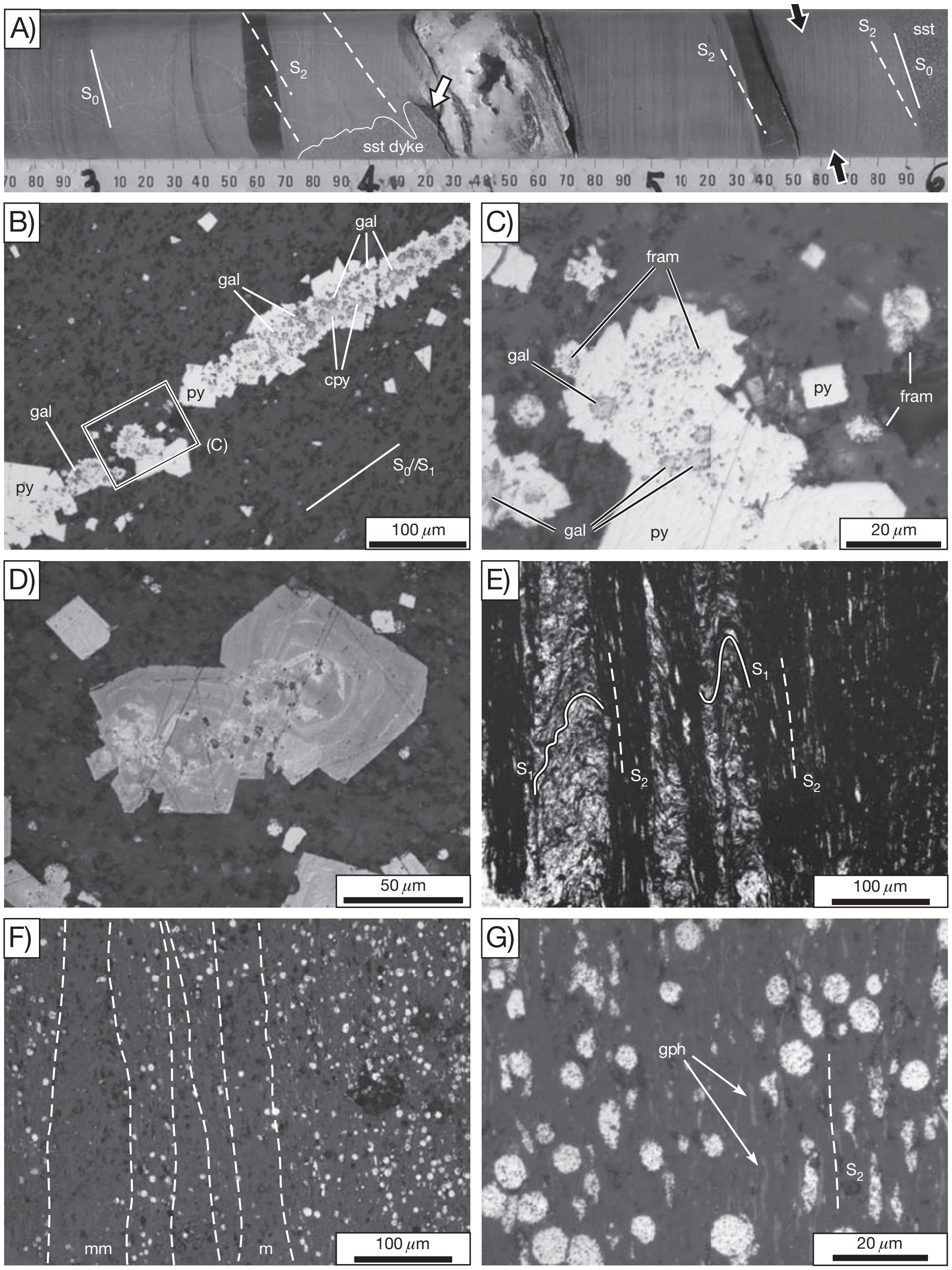

FIG. 9. A. Bedding-parallel quartz-carbonate shear vein in thinly bedded shale, siltstone, and sandstone. Fosterville drill hole RHD019, 161.27–161.6 m (see Fig. 5C for location). Bedding (S_0) and the axial planar cleavage (S_2) indicated by the solid and dashed lines, respectively. Thin white line to the left of the vein marks the edge of a sandstone dike, possibly rooted into the sandstone bed (sst) ~10 cm below the vein. Black and white arrows denote the locations of samples RHD019_161.56 m and 61.42 m, illustrated in parts (B)-(D) and (E)-(G), respectively. B. Reflected-light photomicrograph of fine-grained euhedral pyrite (py) overgrowths on elongate bedding-parallel aggregate of framboidal pyrite. Framboidal pyrite in the cores of these grains is extensively replaced by galena (gal) and chalcopyrite (cpy). C. Detail from (B). D. Reflected-light photomicrograph showing oscillatory zoning in euhedral pyrite that overgrows a small cluster of framboidal pyrite and galena. Zoning is highlighted by variations in degree of natural tarnish. E. and F. Plane-polarized and reflected-light photomicrographs showing detail from discontinuous dark band (indicated by white arrow in A) at the hanging-wall contact of the shear vein. Framboidal pyrite is well developed in the S_2 cleavage domains but largely absent from the intervening microlithons (m) where the bedding-parallel foliation S_1 is preserved. G. Reflected-light photomicrograph of cleavage domain. Ovoid to lenticular aggregates of pyrite microcrystals aligned with S_2 are interpreted as flattened originally spheroidal framboids. Small grains of graphite (gph) are also aligned with S_2.

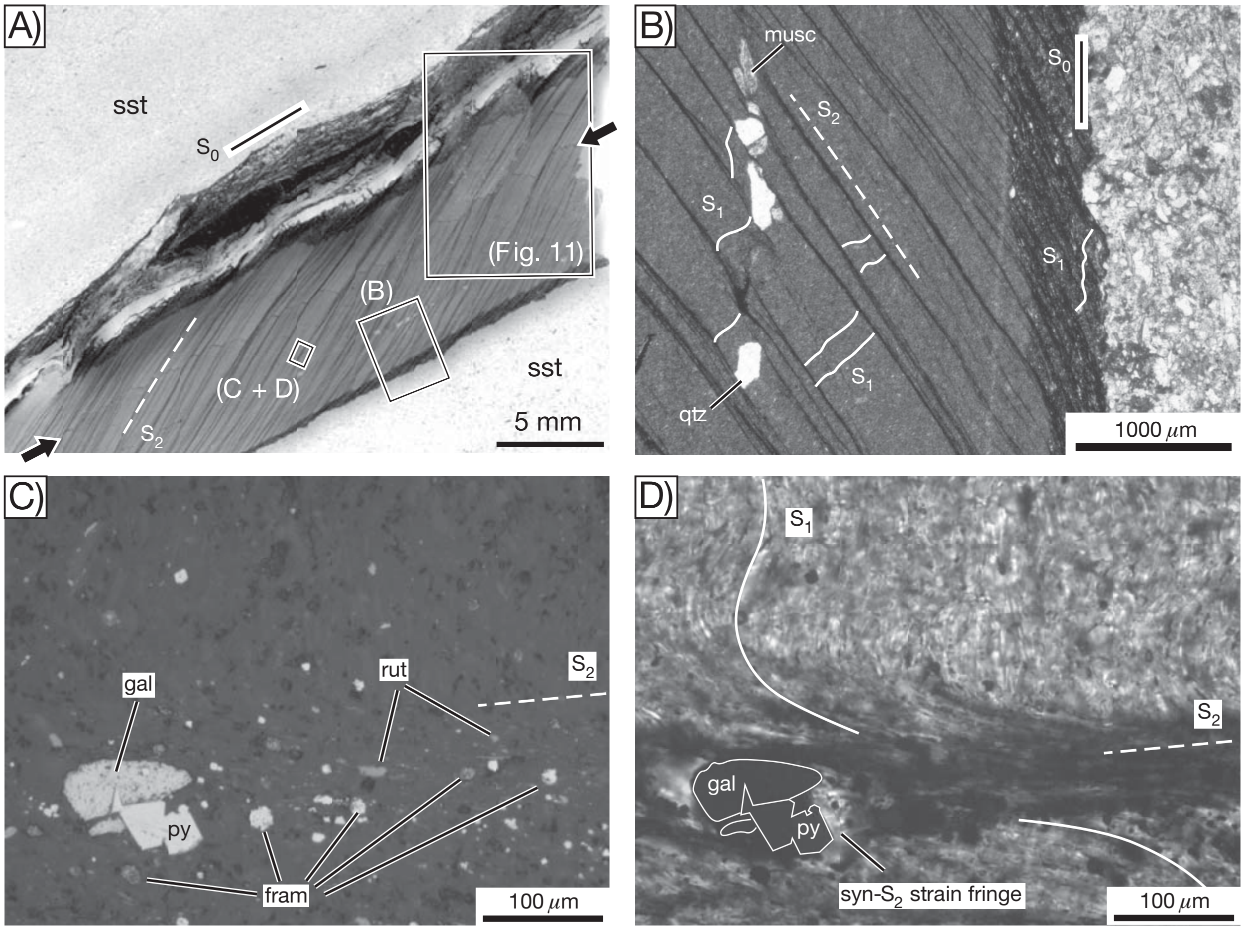

FIG. 10. A. Thin shale and quartz-filled shear vein between thicker sandstone (sst) beds with thin bedding and/or S_1 parallel pyrite trails (e.g., between black arrows) overprinted by S_2. Locations of Figure 11 and photomicrographs in parts (B), (C), and (D) are indicated. Fosterville sample GT8_94.4 m (scan of thin section). B Plane-polarized light photomicrograph showing geometric relationships between S_0, S_1, and S_2 at the base of the shale layer. S_1 appears oblique to S_0 because a single limb of the microfolds is preserved in the microlithons (e.g., Kraus, 2000). The discontinuous band of quartz (qtz) and muscovite (musc) grains are remnants of a thin bedding-parallel vein that was largely removed by dissolution during development of both S_1 and S_2. C. Reflected-light photomicrograph of galena (gal), euhedral pyrite (py), framboidal pyrite (fram), and rutile (rut) along S_2. D. Plane-polarized light photomicrograph of same field of view as (C) showing reorientation of S_1 across the S_2 cleavage domain and syn-S_2 quartz-filled strain fringes adjacent to larger sulfide grains.

the shale were determined (Fig. 12). Element maps on the left in Figure 12 show the total variation in counts for each isotope, whereas maps on the right show the ratio of counts for each isotope divided by counts for ^{49}Ti. Except for a few small zircon(?) crystals (small bright spots in Zr/Ti map), there is little variation in the Ti/Zr ratio across the analyzed area, suggesting both elements were essentially immobile during cleavage formation, at least on scales larger than a few tens of microns (see also Glasson and Keays, 1978).

On average, Ti concentrations along S_2 are ~2.7× higher than those in the adjacent microlithons (Fig. 12), equating to a volume loss of 63 percent from the cleavage domains (Fig. 13). Overall volume loss is <20 percent considering S_2 domains comprise <30 percent of the shale. This estimate is similar to that of Glasson and Keays (1978), who determined ca. 50 percent volume reduction from cleavage domains in similarly deformed strata at the western margin of the Bendigo zone. Magnesium, Mn, Si, Al, and Fe are all depleted from the cleavage domains, suggesting a breakdown of phyllosilicates (±Fe oxides?) during cleavage development liberated Ti and Fe for the development of rutile and pyrite, respectively. In contrast, normally mobile elements such as Sb, As, Ag, Au, Mo, and Pb are concentrated (most likely in pyrite or other sulfides) along the S_2 domains. The relatively high Pb/Ti ratio of the S_2 domains suggests the addition of externally sourced Pb, consistent with the apparent restriction of galena to these domains (e.g., Fig. 10C).

Trace element composition of framboidal pyrite at Fosterville

Trace element compositions of framboidal pyrite in the Fosterville samples were determined by LA-ICPMS (Table 1). Scatter plots for selected trace elements are shown in Figure 14. For comparison, compositional data for two pre-S_2 pyrite nodules (samples GT8_23.2 m and DALD017_66.28) are also provided (Table 1, Fig. 14). Notwithstanding the problems in obtaining truly representative trace element data for very fine grained pyrite (see previous), patterns in laser ablation data similar to those illustrated in Figure 3 indicate

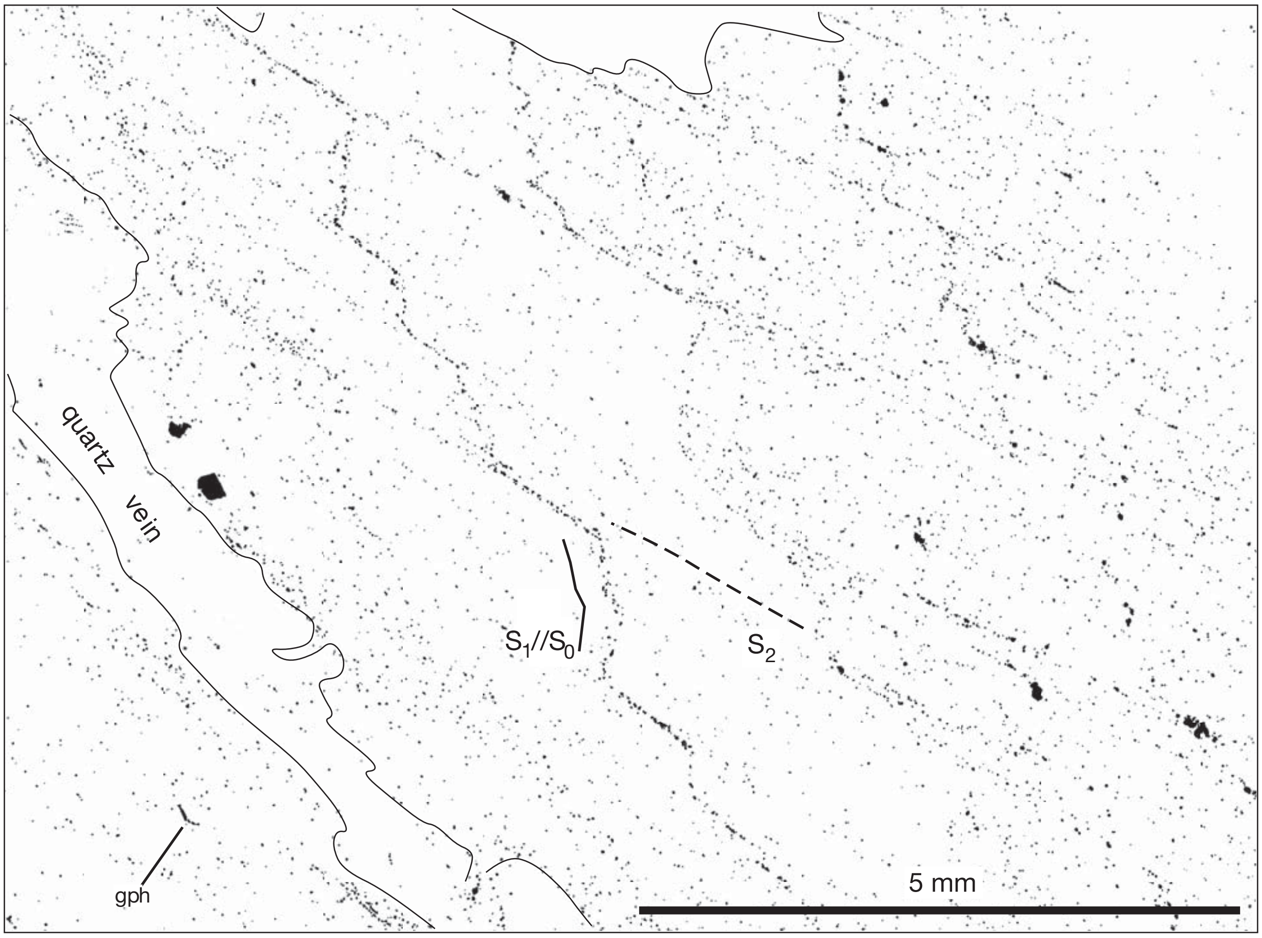

FIG. 11. Pyrite distribution (black spots) across part of the shale layer illustrated in Figure 10A. Image produced from stitched mosaic of twenty-five 2- × 1.5-mm (5×) reflected-light photomicrographs delineating grains down to ca. 5-μm diam. Threshold levels were adjusted so that only the most highly reflective phases (predominantly pyrite) were visible. To enhance visibility at the scale of reproduction used here, 2-pixel-wide layer added to all reflective grains. Although it was not possible to exclude all grains other than pyrite by the threshold method used (and still retain visibility of most pyrite), crosschecking against the thin section indicates that the figure accurately reflects the pyrite distribution. While most pyrite largely predates S_2, additional pyrite growth during cleavage development is indicated by anomalous concentrations of pyrite along the cleavage and a slight coarsening of earlier S_1 parallel pyrite aggregates where realigned parallel to S_2.

that (except for Al, V, Th, and U) elements listed in Table 1 generally vary sympathetically with Fe, suggesting their inclusion in pyrite, or show maximum concentrations coincident with higher proportions of pyrite, suggesting they reside in either coprecipitated, infill, or replacive phases.

The results indicate considerable variation in the trace element content of the framboidal pyrite, although it is generally more enriched than spatially related pyrite nodules and disseminated fine-grained euhedral pyrite (see also Raiswell and Plant, 1980; Large et al., 2007). Syn- to late-S_2 framboidal pyrite in sample RHD019_161.42 m is significantly more enriched in Au, As, Sb, Ni, and Co than that formed prior to the early stages of cleavage development (including that in sample RHD019_161.56 m, <20 cm away; Fig. 14, Table 1). Unfortunately, in the only sample clearly containing both pre- and syn-S_2 framboidal pyrite (sample GT8_94.4 m), the younger framboids are all too small and sparsely distributed along S_2 to permit meaningful compositional analyses by LA-ICPMS.

Pb isotope composition of early-formed sulfides at Fosterville

Meffre et al. (2008) and Woodhead et al. (2009) show that the Pb isotope systematics of pyrite containing several tens to several thousands of ppm Pb (e.g., most preore-stage pyrite at Fosterville) can be effectively characterized by LA-ICPMS, providing additional constraints on age and crystallization sequence. However, in situ Pb isotope analysis of very fine grained pyrite is potentially problematic due to Pb contributions from the surrounding matrix (Meffre et al., 2008). Owing to the relatively large laser beam diameters used for the Pb isotope analyses, matrix typically constitutes a high proportion (i.e., >50%) of the material analyzed, even for relatively dense aggregates of framboidal pyrite. Thus to help evaluate the influence of matrix Pb in such cases, the Pb content and isotopic composition of the matrix in two framboid-rich samples (RHD019_161.42 m and SPD213_351.90 m) were also determined.

The Pb contents and isotopic compositions of framboidal pyrite in sample RHD019_161.56 m could not be directly

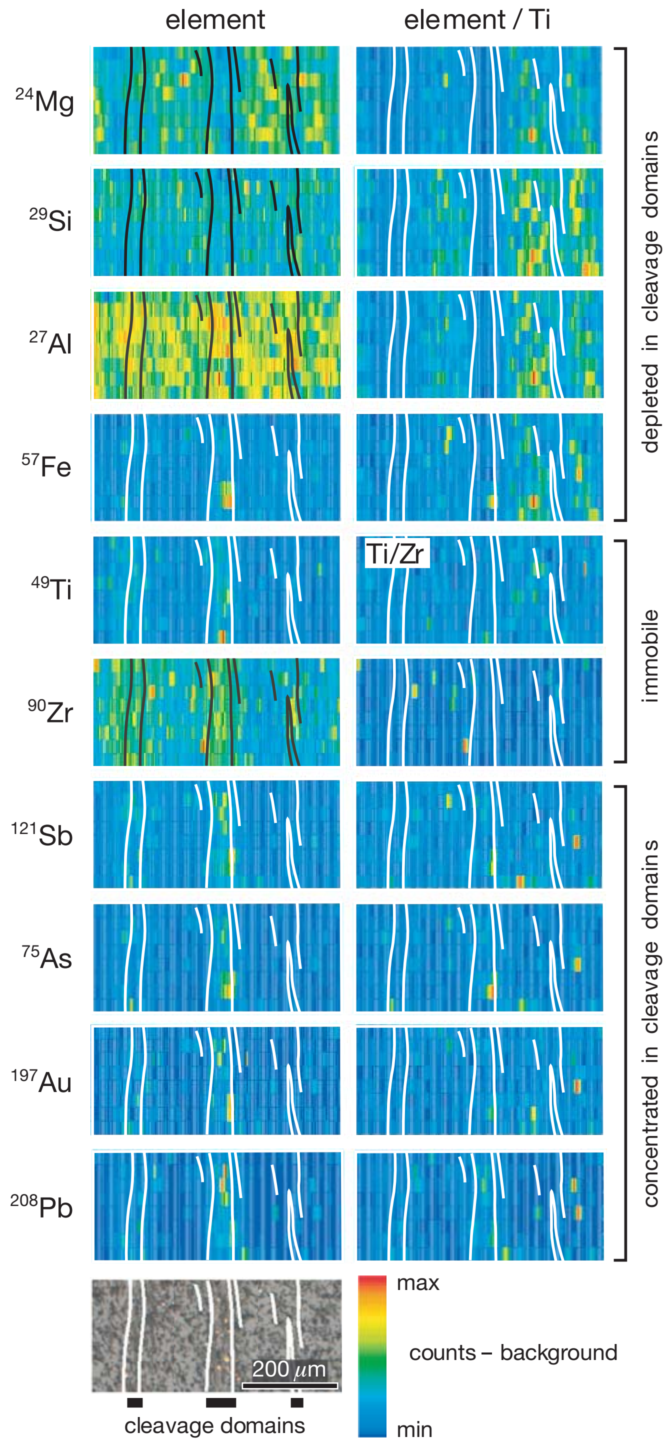

FIG. 12. Laser ablation ICP-MS maps showing variations in element abundance in part of the shale layer illustrated in Figure 10A, compiled from eight adjacent 30- × 540- m line scans with ca. 160 readings per line. The map covers several microlithons and cleavage domains in an area of relatively low pyrite density, away from obvious S_0 and S_1 parallel pyrite-rich lamellae. Maps on left show total variation in counts for each isotope (rolling average of three readings), whereas maps on the right show counts for each isotope divided by those for ^{49}Ti (assumed immobile). Magnesium, Si, Al, and Fe are moderately to significantly depleted, relative to Ti, along S_2 domains, whereas Sb, As, Ag, Au, Pb, and Ag, Mo (not shown) are slightly to significantly enriched.

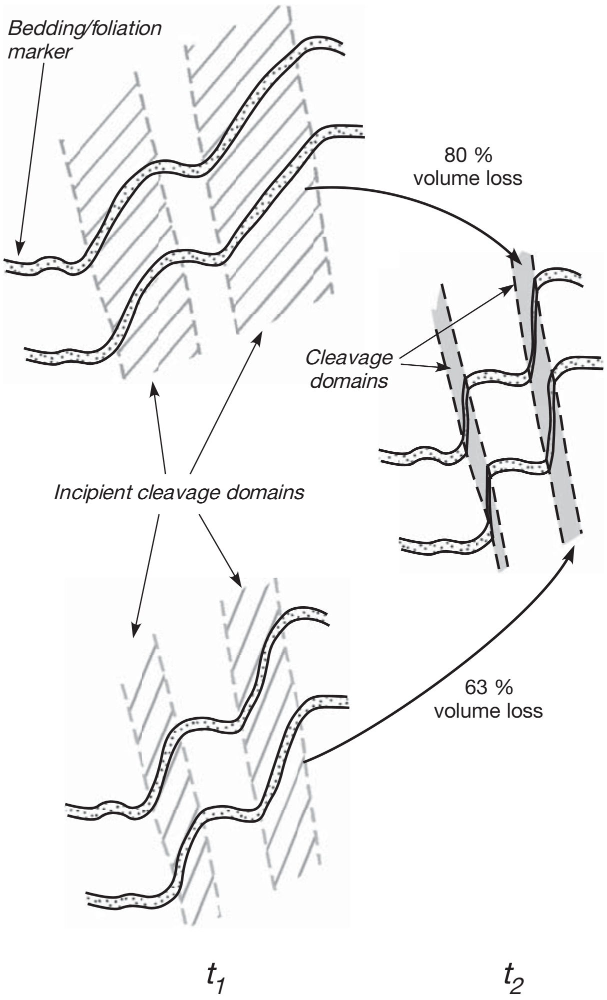

FIG. 13. Total volume loss from cleavage domains can not be determined from the final geometry of fabric elements. This cartoon shows two different deformation paths that produce the same final geometry of fabric elements. Greater volume loss from cleavage domains in the upper example reflects the earlier onset of localized dissolution during microfolding.

determined due to common infill and replacement by galena. Nonetheless, the Pb isotope composition of the galena (determined by solution ICPMS, see "Methods") constrains the minimum age of framboid formation in this sample. Pb isotope data was also obtained for two pre-S_2 pyrite nodules (samples DALD017_66.28 m and GT8_23.2 m) that overgrow (or replace) earlier clusters of framboidal pyrite (e.g., Fig. 7B).

Weighted mean Pb isotope ratios for the sulfides are summarized on conventional ^{207}Pb/^{204}Pb-^{206}Pb/^{204}Pb diagrams in Figure 15. Results are summarized in Table 2 (for tabulation of all results see electronic attachment). Similar results for pre-S_2 pyrite nodules in samples DALD017_66.28 m and GT8_23.2 m were obtained using both the quadrupole and MC instruments, although only the more precise MC-ICPMS data are plotted in Figure 15. Data for these samples and the galena in sample RHD019_161.56 m all plot on the 450 Ma crust-mantle mixing isochron for the eastern Lachlan orogen (Carr et al., 1995), close to the crustal end-member composition (Fig. 15A). Lead in framboidal pyrite in samples

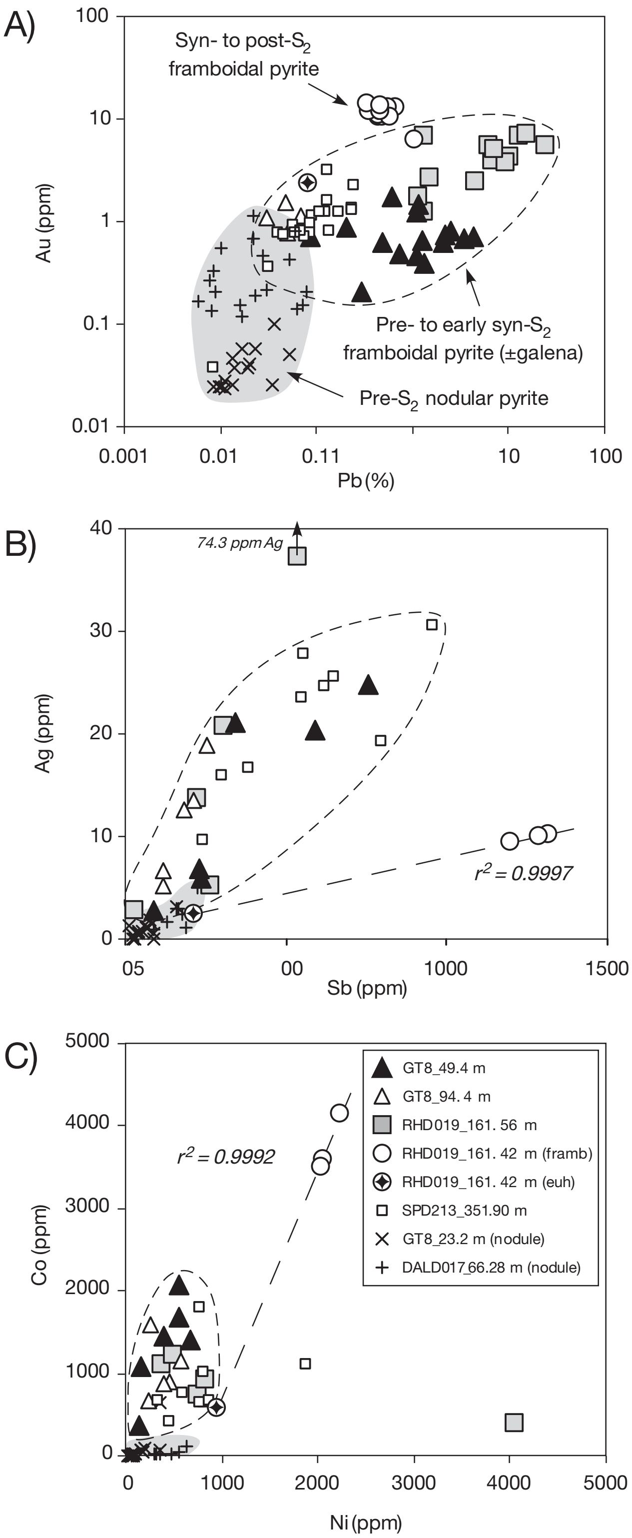

FIG. 14. Scatter plots of selected LA-ICPMS trace element data for framboidal and other early-formed pyrite at Fosterville. A. Au vs. Pb. B. Ag vs. Sb. C. Co vs. Ni. See (C) for key to symbols. Although from beds less than 15 cm apart, framboidal pyrite in samples RHD019_161.42 m and RHD019_161.56 m have very different trace element compositions. The interpreted syn-S$_2$ framboids in sample RHD019_161.42 m are more strongly enriched in Au, Sb, Ni, and Co than those formed prior to S$_2$ in sample RHD019_161.56 m. The high Pb contents of framboidal pyrite aggregates in samples GT8_49.4 m and RHD019_161.56 m are due to later overgrowths and replacement by galena.

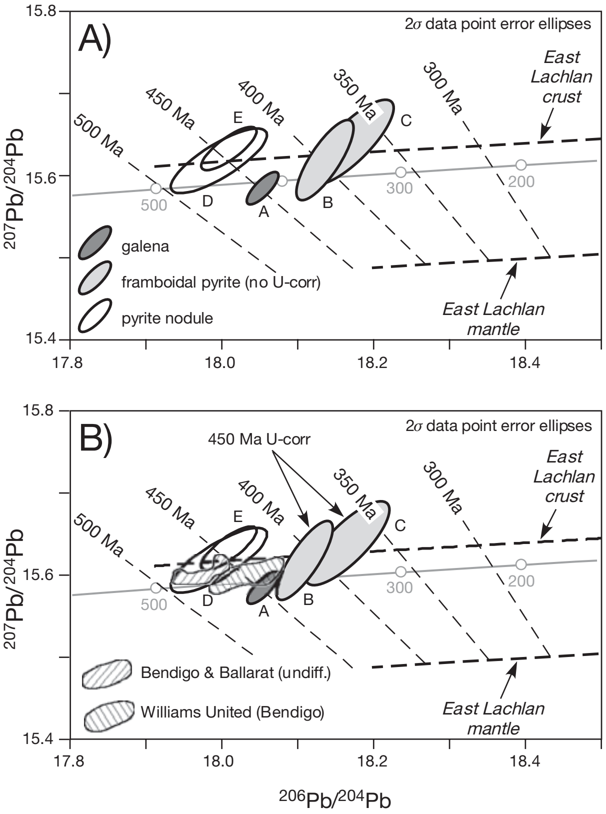

FIG. 15. A. Conventional ^{207}Pb/^{204}Pb vs. ^{206}Pb/^{204}Pb plot showing range in Pb isotope composition for pre- to syn-S$_2$ sulfides at Fosterville. A. Pre- or early syn-S$_2$ galena (solution ICPMS, sample RHD019_161.56 m). B. Syn-S$_2$ framboidal pyrite (LA Quad-ICPMS, sample RHD019_161.42 m). C. Pre- or early syn-S$_2$ framboidal pyrite (LA Quad-ICPMS, sample SPD213_351.90 m). D. and E. Pre-S$_2$ pyrite nodules (LA MC-ICPMS, samples DALD017_66.28 m and GT8_23.2 m). Thick dashed lines are crust and mantle Pb evolution curves and thin dashed lines are mixing isochrons for the eastern Lachlan orogen after Carr et al. (1995). Lead crustal growth curve of Stacey and Kramers (1975) shown in gray. B. As for (A) but with 450 Ma U correction applied to quadrupole LA-ICPMS Pb isotope data for framboidal pyrite samples (B) and (C). U corrections to MC ICPMS data for pre-S$_2$ pyrite nodules (D) and (E) are likely to be negligible based on quadrupole LA ICPMS data for these samples (Table 2). Range in initial Pb isotope ratios for reef-hosted sulfides from Ballarat and Bendigo goldfields (Andrew et al., 2002) shown for comparison.

RHD019_161.42 m (syn- to post-S$_2$) and SPD213_351.90 m (pre- to early syn-S$_2$) is more radiogenic but also plots close to the crustal Pb curve (Fig. 15). Both the quadrupole and MC data show a greater spread in ^{206}Pb/^{204}Pb ratios for framboid-rich aggregates than for the pyrite nodules (Fig. 16), suggesting matrix Pb contribution may be more significant for the framboidal pyrite.

Matrix contributions to pyrite Pb isotope compositions: For the quadrupole instrument data, the relative proportions of (framboidal) pyrite and matrix analyzed were estimated from the measured Al/Fe ratios. This indicates matrix typically constitutes 50 to 80 percent of the material ablated (see Appendix), consistent with visual estimates. Because it represents such a high proportion of the material analyzed, the Pb content and isotopic composition of the matrix must be determined in order to evaluate its likely impact on the apparent Pb isotope composition of the framboidal pyrite.

TABLE 2. Summary of Fosterville Pb Isotope Data

Sample/analysis no.	Inst.[1]	Type[1]	Not corrected for U 206/204	± 1σ	207/204	± 1σ	208/204	± 1σ	450 Ma U correction 206/204	± 1σ	207/204	± 1σ	208/204	± 1σ
GT8 (23.2 m), Fosterville gold mine														
Wtd av (13)[2]	Quad	Pre-S_2 py nodule	17.96	0.03	15.60	0.02	38.04	0.06	17.95	0.03	15.60	0.02	38.03	0.05
Wtd av (5)	MC	Pre-S_2 py nodule	18.01	0.15	15.63	0.02	38.08	0.03						
DALD017 (66.28 m), Daly's Hill area, Fosterville														
Wtd av (12)	Quad	Pre-S_2 py nodule	17.99	0.04	15.59	0.03	37.95	0.07	17.97	0.04	15.59	0.03	37.94	0.07
Wtd av (4)	MC	Pre-S_2 py nodule	18.00	0.03	15.62	0.02	38.04	0.04						
RHD019 (61.56 m), O'Dwyers pit area, Fosterville														
Av (10)	Soln[3]	Pre-S_2 galena	18.05	0.01	15.59	0.01	37.96	0.03						
RHD019 (161.42 m), O'Dwyers pit, Fosterville														
Wtd av (9)	Quad	Syn-S_2 fram	18.13	0.02	15.62	0.02	38.10	0.06	18.11	0.02	15.62	0.02	37.98	0.04
SPD213 (391.90 m), Fosterville gold mine														
Wtd av (11)	Quad	Pre-/syn-S_2 fram	18.17	0.02	15.64	0.02	38.00	0.06	18.17	0.02	15.64	0.02	38.00	0.06

[1] Abbreviations used in table: Inst. = instrument, Quad = quadrupole ICP-MS, MC = multicollector ICP-MS, fram = framboidal pyrite, py = pyrite

[2] Number of analyses used for weighted averages shown in brackets

[3] Solution ICP-MS analyses performed on quadrupole ICP-MS

Quadrupole LA-ICPMS analyses of the matrix, in areas largely or entirely devoid of pyrite in samples RHD019_161.42 m and SPD213_351.90 m yield imprecise but highly radiogenic Pb isotope compositions (Fig. 16). Even when analyzed with the maximum beam diameter (i.e., 110 μm), Pb counts for the matrix were below the optimum range for isotopic characterization on this instrument, suggesting Pb contents <100 ppm (e.g., Meffre et al., 2008). Whole-rock geochemical data indicate carbonaceous and sericitic layers in the sequence adjacent to sample SPD213_351.90 m contain ca. 30 and 50 ppm Pb, respectively (Table 3). Although neither the Pb content nor isotopic composition of the matrix in these samples is particularly well constrained, modeling data for sample RHD019_161.42 m based on best estimates of these parameters suggests matrix-derived Pb only contributes significantly to the measured Pb isotope composition for two analyses in which framboidal pyrite constitutes <10 percent of the ablated material (see Appendix, Table 4).

Lead isotope data for sample SPD213_351.90 m was predominantly obtained from dense clusters of framboidal pyrite overgrown by euhedral pyrite (e.g., Fig. 7C). Aluminum to Fe ratios for these analyses indicate that nonpyritic matrix constitutes <14 percent of the analyzed material (Table 4C) and is unlikely to contribute significantly to the measured Pb isotope compositions. Data for a densely clustered framboid aggregate lacking euhedral pyrite overgrowths (i.e., analysis AU29E09, ~44% nonpyritic matrix, see Table 4C) are indistinguishable from that for aggregates overgrown by euhedral pyrite, suggesting the overgrowths are either of similar Pb isotope composition or do not contribute significantly to the measured values.

Uranium corrections for quadrupole LA-ICPMS data: The quadrupole LA-ICPMS data were also corrected for Pb produced by radioactive decay in U-, Th-bearing mineral inclusions (e.g., Meffre et al., 2008, see Appendix). Assuming a maximum pyrite crystallization age of 450 Ma shifts the Pb isotope composition of framboidal pyrite in sample RHD019_161.42 m to slightly less radiogenic values but makes negligible difference to results for pyrite in the other samples (Fig. 15B, Table 2). It is not possible to correct the MC-ICPMS data because the instrument configuration used for this study does not allow for the simultaneous measurement of U, Th, and Pb.

Discussion

Concentrations of framboidal pyrite along (1) posthydrocarbon generation stylolites and (2) later hydrothermal veins in Upper Devonian sedimentary rocks of the northern Carlin trend, as well as (3) in narrow sulfidic halos to bedding-parallel shear veins in Lower Ordovician turbidites at Fosterville, central Victoria, indicate that framboid formation is not restricted to surficial environments and may occur, in favorable microniches, over a considerable depth range in the upper crust. The similarity in the size and internal morphology of framboids formed in various settings suggests controls on framboid development may be common to all settings.

Framboidal pyrite concentrations along dissolution surfaces, such as stylolites and cleavages, may be explained either by preferential crystallization along these surfaces or the concentration of existing, relatively insoluble minerals as

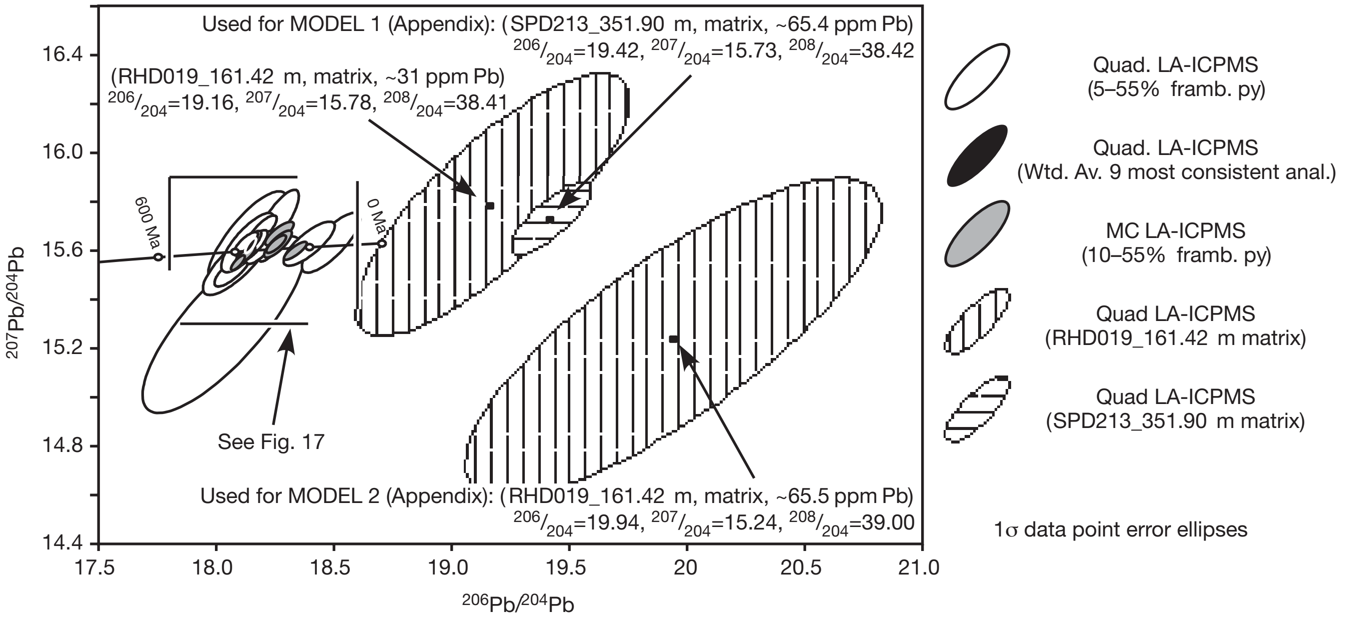

FIG. 16. ^{207}Pb/^{204}Pb vs. ^{206}Pb/^{204}Pb plot showing quadrupole and MC LA-ICPMS data (1 error ellipses) for framboidal pyrite in sample RHD019_161.42 m. The large spread in ^{206}Pb/^{204}Pb ratios is interpreted to reflect variations proportions of more radiogenic matrix Pb in the analyses. The approximate Pb isotope compositions of the shale matrix in this sample (vertical hatch) and in sample SPD213_351.90 m (horizontal hatch) were used to assess the likely influence of matrix Pb on the apparent Pb isotope compositions of the pyrite (see Appendix).

dissolution proceeds (Gray, 1979; Gray and Durney, 1979). The latter process clearly accounts for some pyrite enrichment along S_2 at Fosterville (e.g., Fig. 11). However, although significant, the ca. 60 percent volume loss estimated for S_2 domains in sample GT8_94.4 m only accounts for a ~3× increase in the amount of pyrite along the cleavage, compared to adjacent microlithons. In this sample, sulfide and particularly framboidal pyrite concentrations along S_2, may exceed those of the microlithons by a factor of ten or more (e.g., Figs. 10C, 11), implying that much of the sulfide precipitated during or after cleavage development. Trace element and Pb isotope compositional differences between framboids with distinct microstructural associations at Fosterville also support precipitation at different times from fluids of different composition (Figs. 14, 15).

Microstructural constraints on framboid formation

Widespread overprinting by soft-sediment slump and differential compaction features indicate that most framboidal pyrite in the upper Popovich Formation on the northern Carlin trend probably formed during sedimentation or shallow-level diagenesis (e.g., Scott et al., in prep.; this study). At Fosterville, however, the intensity of grain-scale deformation generally precludes the recognition of similar features (if originally present), and the timing of initial framboid development is more equivocal. Cleavage overprinting relationships indicate most formed either early during or before development of S_2 (e.g., Figs. 7, 8, 11) and thus no later than the earliest stages of regional folding. However, this does not necessarily imply a syngenetic or early diagenetic origin.

Overprinting relationships between framboidal and other early-formed sulfides and the bedding-parallel mica fabric (S_1) at Fosterville are partly obscured by later cleavage development. However, in general, there appears to be little change in either S_1 intensity or orientation in the matrix around either pre-S_2 pyrite nodules or the larger aggregates of framboidal pyrite, nor are S_1 parallel strain fringes developed at their margins. Even where S_1 is strongly developed

TABLE 3. Whole-Rock and LA-ICPMS Constraints on Matrix Composition

	Whole-rock data		Semiquantitative LA-ICPMS matrix analysis		
	Carbonaceous bed (SPD213_352.32)	Sericitic bed (SPD213_352.32)	SPD213_351.90 (Model 1)	RHD019_161.42	RHD019_161.42 (Model 2)
Al (ppm)	62,800	90,000	62,800[#] (= Al_{matrix})	90,000[†] (= Al_{matrix})	90,000[†] (= Al_{matrix})
Fe (ppm)	38,400	40,400	42,880 (= Fe_{matrix})	16,440 (= Fe_{matrix})	13,300 (= Fe_{matrix})
Pb (ppm)	49	29	65.4 (= Pb_{matrix})	65.5 (= Pb_{matrix})	31.0 (= Pb_{matrix})
Tl (ppm)	14.8	21.9	12.1	45.0	18.9
U (ppm)	11.2	15.2	19.5	8.0	6.3
Integration interval	N/A	N/A	34–89 s (AU29E14)	34–42 s (AU29C07)	47–77 s (AU29C07)

Notes: LA-ICPMS data quantified assuming Al concentrations equal to those in sample SPD213_352.32: carbonaceous layer ([#]) and sericitic layer ([†])

TABLE 4. Matrix Pb Corrections to Pb Isotope Determinations for Framboidal Pyrite

A. Sample number RHD019 (161.42 m), Model 1, matrix Pb isotope composition: ^{206}Pb/^{204}Pb = 19.42, ^{207}Pb/^{204}Pb = 15.73, ^{208}Pb/^{204}Pb = 38.42

		Measured ppm			Matrix proportion			Measured ratios		Recalculated pyrite Pb isotope ratios							
										90 ppm Pb in matrix		70 ppm Pb in matrix		50 ppm Pb in matrix		30 ppm Pb in matrix	
Analysis	Framboid abundance	Al (ppm)	Fe (ppm)	Pb (ppm)	Al/Fe	% matrix	% framb	206/204	207/204	206/204	207/204	206/204	207/204	206/204	207/204	206/204	207/204
AU29C01	High	184794	465000	4453.4	0.397	69	31	18.11	15.62	18.09	15.63	18.10	15.63	18.10	15.63	18.11	15.63
AU29C02	High	194946	465000	4893.7	0.419	70	30	18.13	15.62	18.11	15.63	18.11	15.63	18.11	15.63	18.12	15.63
AU29C03	High	158350	465000	5220.1	0.341	65	35	18.06	15.52	18.04	15.52	18.04	15.52	18.04	15.52		
AU29C04	High	184199	465000	5517.8	0.396	69	31	18.14	15.61	18.12	15.62	18.12	15.62	18.13	15.61		
AU29C05	Moderate	296653	465000	4396.5	0.638	79	21	18.18	15.68	18.16	15.68	18.16	15.68	18.16	15.68		
AU29C06	Low	90000	49806	424.3	1.807	93	7	18.38	15.62	18.03	15.71	18.13	15.69	18.17	15.68	18.29	15.65
AU29C07a	Py-free matrix	90000	16436	65.5	5.476	100	0	19.94	15.24	N/A	N/A	N/A	N/A	N/A	N/A	N/A	N/A
AU29C08	Moderate	361376	465000	3608.7	0.777	82	18	18.12	15.63	18.09	15.64	18.10	15.63	18.10	15.63		
AU29C09	High	167332	465000	6771.3	0.360	67	33	18.22	15.61	18.20	15.61	18.21	15.61	18.21	15.61		
AU29C10	High	218891	465000	5567.2	0.471	73	27	18.18	15.61	18.16	15.62	18.17	15.62	18.17	15.61		
AU29C11	Single framb	2	465000	10537.3	0.000	0	100	18.02	15.29	18.02	15.29	18.02	15.29	18.02	15.29		
AU29C12	High	74068	465000	4661.1	0.159	46	54	18.12	15.65	18.11	15.65	18.11	15.65	18.11	15.65		
AU29C13	High	142155	465000	5784.3	0.306	63	37	18.25	15.72	18.23	15.73	18.23	15.73	18.24	15.73		
AU29C14	High	224034	465000	4750.4	0.482	73	27	18.07	15.55	18.05	15.55	18.05	15.55	18.06	15.55		
AU29C15	Low	90000	39102	278.0	2.302	95	5	18.48	15.63	17.89	15.79	18.06	15.74	18.14	15.72	18.34	15.67

B. Sample number RHD019 (161.42 m), Model 2, matrix Pb isotope composition: ^{206}Pb/^{204}Pb = 19.94, ^{207}Pb/^{204}Pb = 15.24, ^{208}Pb/^{204}Pb = 39.00

		Measured ppm			Matrix proportion			Measured ratios		Recalculated pyrite Pb isotope ratios							
										85 ppm Pb in matrix		65 ppm Pb in matrix		55 ppm Pb in matrix		25 ppm Pb in matrix	
Analysis	Framboid abundance	Al (ppm)	Fe (ppm)	Pb (ppm)	Al/Fe	% matrix	% framb	206/204	207/204	206/204	207/204	206/204	207/204	206/204	207/204	206/204	207/204
AU29C01	High	184794	465000	4453.4	0.397	69%	31%	18.114	15.624	18.091	15.629	18.096	15.627	18.099	15.627	18.108	15.625
AU29C02	High	194946	465000	4893.7	0.419	70%	30%	18.129	15.624	18.107	15.629	18.112	15.628	18.115	15.627	18.123	15.626
AU29C03	High	158350	465000	5220.1	0.341	65%	35%	18.056	15.515	18.037	15.519	18.041	15.518	18.044	15.517		
AU29C04	High	184199	465000	5517.8	0.396	68%	32%	18.139	15.612	18.120	15.616	18.125	15.615	18.127	15.615		
AU29C05	Moderate	296653	465000	4396.5	0.638	78%	22%	18.182	15.678	18.155	15.685	18.162	15.683	18.165	15.682		
AU29C06	Low	90000	49806	424.3	1.807	93%	7%	18.383	15.624	18.032	15.714	18.126	15.690	18.172	15.678	18.294	15.647
AU29C07a	Py-free matrix	90000	13313	31.1	6.760	100%	0%	19.943	15.240	N/A	N/A	N/A	N/A	N/A	N/A	N/A	N/A
AU29C08	Moderate	361376	465000	3608.7	0.777	82%	18%	18.122	15.629	18.087	15.636	18.096	15.635	18.099	15.634		
AU29C09	High	167332	465000	6771.3	0.360	66%	34%	18.219	15.606	18.205	15.608	18.208	15.607	18.210	15.607		
AU29C10	High	218891	465000	5567.2	0.471	72%	28%	18.183	15.612	18.163	15.617	18.167	15.616	18.170	15.615		
AU29C11	Single framb	2	465000	10537.3	0.000	0%	100%	18.018	15.291	18.018	15.292	18.018	15.292	18.018	15.292		
AU29C12	High	74068	465000	4661.1	0.159	46%	54%	18.122	15.649	18.107	15.652	18.110	15.651	18.112	15.651		
AU29C13	High	142155	465000	5784.3	0.306	62%	38%	18.247	15.723	18.231	15.728	18.235	15.727	18.237	15.726		
AU29C14	High	224034	465000	4750.4	0.482	73%	27%	18.071	15.545	18.047	15.550	18.052	15.549	18.055	15.548		
AU29C15	Low	90000	39102	278.0	2.302	95%	5%	18.476	15.628	17.886	15.792	18.060	15.744	18.141	15.721	18.340	15.666

TABLE 4. (*Cont.*)

C. Sample number SPD213 (391.90 m), Model 1, matrix Pb isotope composition: $^{206}Pb/^{204}Pb = 19.42$, $^{207}Pb/^{204}Pb = 15.73$, $^{208}Pb/^{204}Pb = 38.42$

		Measured ppm			Matrix proportion			Measured ratios		Recalculated pyrite Pb isotope ratio 65 ppm Pb in matrix	
Analysis	Framboid distribution	Al (ppm)	Fe (ppm)	Pb (ppm)	Al/Fe	% matrix	% framb	206/204	207/204	206/204	207/204
AU29E01	Dense cluster in nodule	3138	465000	911.9	0.007	5	95	18.12	15.62	18.12	15.62
AU29E02	Dense cluster in nodule	2566	465000	1233.1	0.006	4	96	18.14	15.54	18.14	15.54
AU29E03	Dense cluster in nodule	9452	465000	1336.7	0.020	13	87	18.28	15.57	18.27	15.57
AU29E04	Nodule	192	465000	113.0	0.000	0	100	19.00	16.33	19.00	16.33
AU29E05	Dense cluster in nodule	2878	465000	1080.8	0.006	4	96	18.00	15.63	18.00	15.63
AU29E06	Dense cluster in nodule	1956	465000	570.2	0.004	3	97	18.17	15.53	18.17	15.53
AU29E07	Dense cluster in nodule	4808	465000	848.9	0.010	7	93	18.12	15.64	18.12	15.64
AU29E08	Dense cluster in nodule	2426	465000	865.1	0.005	4	96	18.17	15.63	18.17	15.63
AU29E09	Dense cluster in matrix	46912	465000	2470.5	0.101	45	55	18.11	15.59	18.09	15.59
AU29E10	Dense cluster in nodule	7749	465000	750.8	0.017	11	89	18.22	15.65	18.20	15.65
AU29E11	Dense cluster in nodule	4821	465000	676.0	0.010	7	93	18.22	15.70	18.22	15.70
AU29E12	Indiv. framb in matrix	6418	465000	1302.8	0.014	9	91	19.15	16.24	19.14	16.24
AU29E13	Dense cluster in nodule	1180	465000	394.2	0.003	2	98	18.09	15.64	18.09	15.64
AU29E14	Matrix	62800	42879	65.5	1.465	100	0	19.40	15.72	N/A	N/A
AU29E01	Dense cluster in nodule	3138	465000	911.9	0.007	5	95	18.12	15.62	18.12	15.62

framboidal pyrite aggregates are not obviously disaggregated boudinaged, or flattened due to S_1 parallel extension, as is locally observed for framboidal pyrite aggregates overprinted by S_2 (e.g., Figs. 8, 9G). This suggests that the framboid aggregates developed along existing fabric planes; perhaps as a result of similar processes to those inferred to account for framboid development along S_2 (see below). Collectively, microstructural relationships and the apparent restriction of well-developed framboidal pyrite aggregates to sulfidic halos around bedding-parallel shear veins, strongly suggest they are genetically related. Most, if not all, significant early sulfide development at Fosterville appears to reflect the episodic discharge of hydrothermal fluids along bedding-parallel slip surfaces formed during folding.

Pb isotope constraints on framboid formation at Fosterville

Previous Pb isotope studies in southeastern Australia provide a basis for evaluating the temporal significance of sulfide Pb isotope data from Fosterville. In the eastern Lachlan orogen, the Pb isotope systematics of Ordovician to Carboniferous mineral deposits are consistent with Pb derivation from either mantle or long-lived crustal reservoirs, or from a mixture of both sources (Carr et al., 1995). While some large-scale heterogeneity in Pb reservoirs across the orogen appears likely, Andrew et al. (2002) found that Pb isotope systematics (and model ages) for sulfides from central and western Victorian gold deposits (western Lachlan orogen) were broadly consistent with the Carr et al. (1995) model.

The 450 to 400 Ma Pb model ages for sulfides formed prior to Early to Middle Devonian gold mineralization at Fosterville (Fig. 15) support their interpreted epigenetic origins. While only broadly indicative of crystallization ages, these Pb model ages overlap with established deformation and mineralization ages in central Victoria (Foster et al., 1998; Foster and Gray, 2000; Vandenberg et al., 2000). The Pb isotope compositions of pre- to early syn-S_2 pyrite nodules (samples DALD017_66.28 m and GT8_23.2 m) and galena (sample RHD019_161.56 m) at Fosterville overlap with the least radiogenic Pb isotope compositions for sulfides from auriferous reefs at Bendigo, 30 km to the west (Fig. 15B, e.g., Bierlein and McNaughton, 1998; Andrew et al., 2002). However, whereas major gold mineralization at Bendigo occurred during the late stages of local fold and cleavage development (ca. 440 Ma, Foster et al., 1998; Arne et al., 2001; Schaubs and Wilson, 2002; Willman, 2007), sulfides with similar Pb isotope compositions at Fosterville formed much earlier during the local fold development. In contrast, syn-S_2 framboidal pyrite at Fosterville (sample RHD019_161.42 m) yielded a distinctly younger Pb model age. Collectively, this data support the previously postulated eastward progression of fold and cleavage development across the Bendigo zone (e.g., Foster et al., 1998; Foster and Gray, 2000).

Not all the Fosterville Pb isotope data are consistent with relative timings based on cleavage overprinting relationships, however. Framboidal pyrite in sample SPD213_351.90 m yielded the most radiogenic (weighted average) Pb isotope composition of any of the samples considered here (Fig. 15, Table 2), yet cleavage overprinting relationships suggest it formed no later than the early stages of S_2 development; before framboidal pyrite in sample RHD019_161.42 m. This discrepancy implies that at least some of the Pb in pyrite from sample SPD213_351.90 m may have been derived from a distinct reservoir that did not evolve along the same growth curve as the dominant source of Pb in pyrite from the other samples.

Implications for framboid formation mechanisms

This paper primarily addresses the where and when of framboid formation, rather than how and why. Nonetheless, relationships documented here do have implications for the processes by which framboidal pyrite forms. In particular, no obvious morphological differences were recognized between framboidal pyrite of syngenetic-early diagenetic origin, and that interpreted have formed during later burial, deformation or hydrothermal alteration. This suggests that crystallization paths were either independent of the geologic environment in which the framboids formed or that different crystallization paths produce a similar range in framboid morphologies.

Ideas about the formation of framboidal pyrite have changed considerably over the last 50 years. Prior to the 1970s, biogenic processes were widely considered critical (Schneiderhöhn, 1923; Love, 1957; Love and Zimmerman, 1961; Rickard, 1970). Subsequent experimental syntheses of framboidal pyrite demonstrate this is not the case (e.g., Berner, 1969; Sweeny and Kaplan, 1973; Wilkin and Barnes, 1996; Butler and Rickard, 2000). However, much of the experimental work (see Ohfuji and Rickard, 2005, for a review) was interpreted to indicate framboid formation involves complex crystallization paths, and the critical role of specific precursors, most notably the magnetic thiospinel, greigite (Fe_3S_4, e.g., Sweeny and Kaplan, 1973; Wilkin and Barnes, 1997). Later experimental work by Butler and Rickard (2000) indicated greigite is also not required and that framboidal pyrite can form directly via the dissolution of solid FeS and subsequent rapid oxidation of the resultant $FeS_{(aq)}$ cluster complexes by aqueous H_2S.

The attainment of very high pyrite supersaturations appears to be critical for the formation of framboidal pyrite (Butler and Rickard, 2000; Ohfuji and Rickard, 2005). The small size, large number (up to 10^6), and uniform morphology of the microcrystals comprising individual framboids suggest nucleation was very rapid, consistent with precipitation from supersaturated solutions (Wilkin and Barnes, 1997; Butler and Rickard, 2000; Ohfuji and Rickard, 2005). Growth of microcrystals is presumably also rapid but limited by nutrient supply. In other words, initially highly supersaturated fluids become undersaturated, with respect to pyrite, as nutrients are depleted by microcrystal growth (Ohfuji and Rickard, 2005).

Rapid oxidation of $FeS_{(aq)}$ by H_2S proposed by Butler and Rickard (2000) provides a mechanism for framboid formation in relatively reduced or anoxic environments where S^{2-} is by far the dominant sulfur species. As the reactants are dissolved phases this also accounts for direct precipitation of framboidal pyrite from pore waters and hydrothermal fluids (e.g., Chen, 1978; Pichler et al., 1999; this study). Experimental work by Butler and Rickard (2000) and studies of framboid distribution in euxinic basins (e.g., Wilkin et al., 1996, 1997) indicate precipitation of framboidal pyrite is favored by comparatively oxidized conditions close to the SO_4^{2-}/S^{2-} "redox" boundary (Ohfuji and Rickard, 2005). Pyrite solubility changes abruptly at this boundary, facilitating development of more highly FeS_2 supersaturated fluids than in reduced (lower Eh) systems with the same total concentrations of Fe and S (Butler and Rickard, 2000; Ohfuji and Rickard, 2005). Butler and Rickard (2000) also predicted that framboid formation may be favored by lower pH conditions, consistent with the intimate association of framboidal pyrite and colloform-textured marcasite in some hydrothermal precipitates (e.g., Fig. 4; Schouten, 1946; Pichler et al., 1999; this study). Marcasite crystallization is interpreted to be indicative of lower pH conditions (i.e., pH <5, Murowchick and Barnes, 1986; Murowchick, 1992).

Due to the finite rates of mineral dissolution, framboidal pyrite is unlikely to form via direct replacement of crystalline materials (Rickard, 1970; Butler and Rickard, 2000). Nonetheless, textural relationships in many of the samples considered here suggest that framboids formed via the partial or selective replacement of their immediate substrate (e.g., Fig. 1B-D). Rickard (1970) suggested such conflicts between textural relationships and inferred crystallization mechanisms could be reconciled if the framboids formed via the rapid pyritization of amorphous organic matter (including spherical organic globules, as modeled by Raiswell et al., 1993) or (H_2S-filled?) vacuoles in the sediment, where the external morphology of the framboids (or framboid aggregates) is partly or entirely controlled by the shape of the precursor.

The requirement of high FeS_2 supersaturations has important hydrological implications for framboid crystallization, as migration of such fluids over geologically significant length scales is not feasible. Supersaturation must be attained at the sites of framboid crystallization. Naturally occurring framboidal pyrite, where present, is generally the earliest form of pyrite precipitated. Where pyrite precipitation continued, framboids are commonly overgrown by, or recrystallized to form, coarser grained euhedral pyrite (e.g., Raiswell and Plant, 1980; England and Ostwald, 1993; Large et al., 2007; Scott et al., in prep.). Only in a few reported cases do framboids appear to have formed again during later stages of pyrite paragenesis (e.g., Chen, 1978; this study).

The transition from framboidal to coarser grained euhedral pyrite has been interpreted to reflect exhaustion of sources of highly reactive Fe in the immediate substrate, with a resultant decrease in the Fe content of pore fluids, requiring longer range Fe transport to the sites of pyrite precipitation (Raiswell and Plant, 1980; Raiswell et al., 1993). The absence of framboidal pyrite formed later during pyrite paragenesis suggests that once sources of highly reactive Fe are depleted, the capacity for generating highly pyrite supersaturated pore fluids is lost in many geologic settings. However, Butler and Rickard (2000) argued that aqueous FeS cluster complexes can potentially form during the dissolution of any Fe-bearing phase. Accordingly, the range of (micro-) environments in which framboidal pyrite may develop (via the crystallization pathway suggested by Butler and Rickard, 2000) is limited only by the requirements that FeS cluster complexes form and, together with H_2S, attain supersaturation. Indeed, Ohfuji and Rickard (2005) noted that to date, all successful laboratory syntheses of large, well-developed pyrite framboids were for experiments conducted at higher temperatures (e.g., 50°–350°C) than generally thought applicable to most framboid formation in nature (i.e., $T < 20°C$). They attribute this to the role of temperature in increasing reaction kinetics and suggest that framboid development is favored where reaction rates are high.

Framboidal pyrite development along dissolution surfaces

The preferential development of framboidal pyrite along stylolites and cleavages in Palaeozoic sedimentary rocks from northeastern Nevada and central Victoria suggests that such features locally provide suitable microenvironments for framboid nucleation at higher temperatures (up to at least those of lower greenschist-facies metamorphic conditions). Despite increased concentrations of pyrite and framboidal pyrite along S_2 in some samples from Fosterville, LA-ICPMS data indicates a net loss of Fe from these domains (Fig. 12). This suggests pyrite development may have been triggered, at least in part, by increased concentrations of Fe in pore waters due to the localized dissolution of Fe-bearing minerals along the cleavage. Reduced S may have been similarly derived from in situ sources (e.g., Glasson and Keays, 1978); however, marked S enrichment and $\delta^{34}S$ zonation in the wall rocks around vein systems at most gold deposits in central Victoria (Stüwe et al., 1988; Cox et al., 1995; Gao and Kwak, 1997; Bierlein et al., 1998, 2000, 2004; Andrew et al., 2002) suggest the introduction of externally derived sulfur (e.g., H_2S-bearing fluids) was also critical to pyrite formation. In this respect, it is noteworthy that Fosterville samples which have the best developed concentrations framboidal pyrite along S_2 were located immediately adjacent to bedding-parallel shear veins.

The likely importance of externally derived sulfur for sulfide development along S_2 is also suggested by the work of Glasson and Keays (1978), who demonstrated that both sulfur and pyrite are generally depleted from cleavage domains in the Castlemaine Group (i.e., at greater distance from the veins). Accordingly, framboid nucleation adjacent to bedding-parallel veins at Fosterville is interpreted to reflect the interaction between locally sourced Fe-enriched pore waters and externally derived H_2S-bearing hydrothermal fluids. In addition, many of the laminated bedding-parallel shear veins in the Castlemaine Group, including those at Fosterville, appear to have provided conduits for migrated hydrocarbons (e.g., Bierlein et al., 2001b). Petroleum, methane and/or H_2S that diffused from the veins into the adjacent wall rocks may have formed bubbles or globules that provided spherical precursors for framboid precipitation (e.g., Rickard, 1970).

Metal enrichment in framboidal pyrite

This and previous studies (e.g., Raiswell and Plant, 1980; Large et al., 2007; Scott et al., in prep.) demonstrate that framboidal pyrite may be significantly enriched in a wide range of trace elements compared to adjacent, later formed and coarser grained pyrite. While this may principally reflect differences in the local trace metal budget at the time of pyrite formation (e.g., Raiswell and Plant, 1980; Scott et al., in prep.), the relatively rapid nucleation of framboidal pyrite may also facilitate greater incorporation of impurities. Defect densities, caused by or capable of accommodating impurities, are likely to be highest where crystal nucleation and growth is rapid such as in framboidal pyrite (e.g., Raiswell and Plant, 1980; Butler and Rickard, 2000). Furthermore, the relatively large surface to volume ratio of framboidal pyrite may enhance sorption of trace elements in comparison to coarser grained pyrite (Raiswell and Plant, 1980; Bostick and Fendorf, 2003).

Overprinting by soft-sediment slump and compaction features suggest that most framboidal pyrite developed in the upper Popovich Formation on the northern Carlin trend is of early diagenetic origin. Accordingly, the consistent stratigraphic variations in trace element composition of framboidal and other early-formed pyrite in these rocks (Scott et al., in prep.) are interpreted to reflect progressive changes in detrital input and the composition or oxidation state of basin bottom waters during sedimentation. However, similar dense clusters of framboidal pyrite adjacent to bedding-parallel veins at Fosterville are interpreted to have formed well after sedimentation, in response to the episodic influx of hydrothermal fluids during regional deformation. In this case, elevated trace metal contents of the framboidal pyrite may have a more exotic origin.

Many of the metals concentrated in framboidal pyrite at Fosterville (e.g., Ag, As, Au, Mo, Pb, Sb) are interpreted to be released from sedimentary rocks during metamorphism, particularly during the transition from greenschist- to amphibolites-facies metamorphic conditions (Pitcairn et al., 2006; Large et al., 2007). Indeed, previous studies suggest that most of these elements were depleted from cleavage domains in the Ordovician shales from central Victoria (Glasson and Keays, 1978). Thus, while some trace elements incorporated into sulfides formed adjacent to bedding-parallel veins may have been partly sourced from the immediate host rocks, others (e.g., Pb enriched relative to immobile Ti in S_2 cleavage domains in sample GT8_94.4. m) are more likely sourced from rocks undergoing higher grade metamorphism at greater depth. Thus, in sedimentary successions that have undergone similar deformation and metamorphic histories to those in central Victoria, sulfide distribution patterns (e.g., see Annels and Roberts, 1989), overprinting criteria, and compositional constraints on framboid formation should all be carefully evaluated before any genetic significance is attached to either its occurrence or metal content.

Conclusions

Overprinting relationships and distribution patterns for framboidal pyrite in the sedimentary host rocks to gold deposits on the Carlin trend, Nevada, and at Fosterville, central Victoria, suggest it is not all of syngenetic or early diagenetic origin. Anomalous concentrations of framboidal pyrite in structures formed during late diagenesis, regional deformation, and late-stage hydrothermal alteration suggest that framboidal pyrite can form over a wide range of conditions in the upper crust and at temperatures up to at least those of lower greenschist-facies metamorphism. In such cases, framboid development may occur tens or hundreds of millions of years after deposition of the host rocks. The similarity of framboids formed in syngenetic and epigenetic settings suggests a single dominant (and presumably simple) crystallization path, such as direct crystallization from dissolved reactants (e.g., Butler and Rickard, 2000; Ohfuji and Rickard, 2005), operates over a considerable depth range in the upper crust.

The development of anomalously metal-rich nodular and framboidal pyrite in the sulfidic halos to hydrothermal veins at Fosterville, central Victoria, has implications for models of basin metallogeny. Similarly enriched framboidal (and other texturally primitive) pyrite in deformed and metamorphosed sedimentary successions elsewhere has been interpreted as evidence for metal enrichment during sedimentation or early diagenesis (e.g., Li et al., 1998; Pitcairn et al., 2006; Large et al., 2007). However, the results of this study highlight the importance of carefully characterizing distributions and microstructural relationships before attaching genetic significance to either the occurrence or metal content of framboidal pyrite.

Acknowledgments

This work was jointly funded by CODES-AMIRA project P923 "Controls on the Formation and Sulfide Trace Element Signatures of Sediment-hosted Gold Deposits" and the ARC Centre of Excellence in Ore Deposits at the University of Tasmania. Assistance provided by Jon Powell (Newmont), Bob Leonardson and Charles Weakly (Barrick Gold Co.) and Neil Norris (Perseverance) with the selection of drill holes for sampling is gratefully acknowledged. David Rickard and Robert Raiswell are thanked for incisive reviews, which have helped us to improve the manuscript.

REFERENCES

Andrew, A.S., Gulson, B.L., Carr, G.R., and Keays, R.R., 2002, Victorian hard-rock gold deposits: Sources and sinks, *in* Phillips, G.N. and Ely, K.S., eds., Victoria undercover – Benalla 2002: Melbourne, CSIRO Division of Exploration and Mining, p. 71–78.

Annels, A.E., and Roberts, D.E., 1989, Turbidite-hosted gold mineralization at the Dolaucothi gold mines, Dyfed, Wales, United Kingdom: Economic Geology, v. 84, p. 1293–1314.

Armstrong, A.K., Theodore, T.G., Oscarso, R.L., Kotlyar, B.B., Harris, A.G., Bettles, K.H., Lauha, E.A., Hipsley, R.A., Griffin, G.L., Abbott, E.W., and Cluer, J.K, 1998, Preliminary facies analysis of Silurian and Devonian autochthonous rocks that host gold along the Carlin trend, Nevada: U.S. Geological Survey Open-File Report 98-338, p. 38–68.

Arne, D.C., Bierlein, F.P., McNaughton, N.J., Wilson, C.J.L., and Morand, V., 1998, Absolute timing constraints of gold mineralisation in central Victoria: New constraints from SHRIMP II analysis of zircon grains from felsic intrusive rocks: Ore Geology Reviews, v. 13, p. 251–273.

Arne, D.C., Bierlein, F.P., Morgan, J.W. and Stein H.J., 2001, Re-Os dating of sulfides associated with gold mineralization in central Victoria, Australia: Economic Geology, v. 96, p. 1455–1459.

Berner, R.A., 1969, The synthesis of framboidal pyrite: Economic Geology, v. 64, p. 383–384.

——1970, Sedimentary pyrite formation: American Journal of Science, v. 268, p. 1–23.

——1984, Sedimentary pyrite formation: An update: Geochimica et Cosmochimica Acta, v. 48, 605–615.

Bierlein, F.P., and McNaughton, N.J., 1998, Pb isotope fingerprinting of mesothermal gold deposits from central Victoria, Australia: Implications for ore genesis: Mineralium Deposita, v. 33, p. 633–638.

Bierlein, F.P., Fuller, T., Stüwe, K., Arne, D.C., and Keays, R.R., 1998, Wall-rock alteration associated with turbidite-hosted gold deposits: Examples from the Palaeozoic Lachlan fold belt in central Victoria, Australia: Ore Geology Reviews, v. 13, p. 345–380.

Bierlein, F.P., Arne, D.C., McKnight, S., Lu, J., Reeves, S., Besanko, J., Marek, J., and Cooke, D., 2000, Wall-rock petrology and geochemistry in alteration halos associated with mesothermal gold mineralization, central Victoria: Economic Geology, v. 95, p. 283–311.

Bierlein, F.P., Arne, D.C., Keay, S.M., and McNaughton, N.J., 2001a, Timing relationships between felsic magmatism and mineralisation in the central Victorian gold province, Southeast Australia: Australian Journal of Earth Sciences, v. 48, p. 883–899.

Bierlein, F.P., Cartwright, I. and McKnight, S., 2001b, The role of carbonaceous "indicator" slates in the genesis of lode gold mineralization in the western Lachlan orogen, Victoria, southeastern Australia: Economic Geology, v. 96, p. 431–451.

Bierlein, F.P., Arne, D.C., and Cartwright, I., 2004, Stable isotope (C, O, S) systematics in alteration haloes associated with orogenic gold mineralization in the Victorian gold province, SE Australia: Geochemistry: Exploration, Environment, Analysis, v. 4, p. 191–211.

Bostick, B.C., and Fendorf, S., 2003, Arsenite sorption on troilite (FeS) and pyrite (FeS_2): Geochimica et Cosmochimica Acta, v. 67, p. 909–921.

Boucher, R.K., Hitchman, S.P., and Allwood, K.J., 2008, Stratigraphic controls on structures and mineralization in central Victoria. 3: Fosterville: Australian Institute of Geoscientists (AIG) News, no. 93, p. 6–9.

Butler, I.B., and Rickard, D., 2000, Framboidal pyrite formation via the oxidation of iron (II) monosulfide by hydrogen sulphide: Geochimica et Cosmochimica Acta, v. 64, p. 2665–2672.

Canfield, D.E., Raiswell R., and Bottrell S., 1992, The reactivity of sedimentary iron minerals towards sulfide: American Journal of Science, v. 292, p. 659–683.

Carr, G.R., Dean, J.A., Suppel, D.W., and Heithersay, P.S., 1995, Precise lead isotope fingerprinting of hydrothermal activity associated with Ordovician to Carboniferous metallogenic events in the Lachlan fold belt of New South Wales: Economic Geology, v. 90, p. 1467–1505.

Chen, T.T., 1978, Colloform and framboidal pyrite from the Caribou deposit, New Brunswick: Canadian Mineralogist, v. 16, p. 9–15.

Cline, J.S., Hofstra, A.H., Muntean, J.L., Tosdal, R.M., and Hickey, K.A., 2005, Carlin-type gold deposits in Nevada: Critical geologic characteristics and viable models: Economic Geology 100th Anniversary Volume, p. 451–484.

Cox, S.F., Sun, S.-S., Etheridge, M.A., Wall, V.J., and Potter, T.F., 1995, Structural and geochemical controls on the development of turbidite-hosted gold quartz vein deposits, Wattle Gully mine, central Victoria, Australia: Economic Geology, v. 90, p. 1722–1746.

Emsbo, P. and Koenig, A.E., 2007, Transport of Au in petroleum: Evidence from the northern Carlin trend, Nevada [abs.]: Society for Geology Applied to Mineral Deposits, Biennial SGA Meeting, 9th, Dublin, Proceedings, p. 695–698.

Emsbo, P., Hutchinson, R.W., Hofstra, A.H., Volk, J.A., Bettles, K.H., Baschuk, G.J., and Johnson, C.A., 1999, Syngenetic Au on the Carlin trend: Implications for Carlin-type deposits: Geology, v. 27, p. 59–62.

Emsbo, P., Hofstra, A.H., Lauha, E.A., Griffin, G.L., and Hutchinson, R.W., 2003, Origin of high-grade gold ore, source of ore fluid components, and genesis of the Meikle and neighboring Carlin-type deposits, northern Carlin trend, Nevada: Economic Geology, v. 98, p. 1069–1105.

England, B.M., and Ostwald, J., 1993, Framboid-derived structures in some Tasman fold belt base-metal sulphide deposits, New South Wales, Australia: Ore Geology Reviews, v. 7, p. 381–412.

Foster, D.A., and Gray, D.R., 2000, Timing of orogenic events in the Lachlan orogen (Discussion): Australian Journal of Earth Sciences, v. 47, p. 813–818.

Foster, D.A., Gray, D.R., Kwak, T.A.P., and Bucher, M., 1998, Chronology and tectonic framework of turbidite-hosted gold deposits in the western Lachlan fold belt, Victoria: $^{40}Ar/^{39}Ar$ results: Ore Geology Reviews, v. 13, p. 229–250.

Fowler, T.J., 1996, Flexural-slip generated bedding-parallel veins from central Victoria, Australia: Journal of Structural Geology, v. 18, p. 1399–1415.

Fowler, T.J., and Winsor, C.N., 1997, Characteristics and occurrence of bedding-parallel slip surfaces and laminated veins in chevron folds from the Bendigo-Castlemaine goldfields: Implications for flexural slip folding: Journal of Structural Geology, v. 19, p. 799–815.

Furley, R.A., 2001, Sequence stratigraphic framework for the Silurian-Devonian Bootstrap limestone, Roberts Mountains, and Devonian Popovich Formations, northern Carlin trend, Elko and Eureka counties, Nevada: Unpublished M.Sc. thesis, Colorado School of Mines, 194 p.

Gao, Z.L., and Kwak, T.A.P., 1997, The geochemistry of wall rock alteration in turbidite-hosted gold vein deposits, central Victoria, Australia: Journal of Geochemical Exploration, v. 59, p. 259–274.

Glasson, M.J., and Keays, R.R., 1978, Gold mobilization during cleavage development in sedimentary rocks from the auriferous slate belt of Central Victoria, Australia: Some important boundary conditions: Economic Geology, v. 73, p. 496–511.

Gray, D.R., 1979, Microstructure of crenulation cleavages— indicator of cleavage origin: American Journal of Science, v. 279, p. 97–128.

Gray, D.R., and Durney, D.W., 1979, Crenulation cleavage differentiation—implications of solution-deposition processes: Journal of Structural Geology, v. 1, p. 73–80.

Halbach, P., Pracejus, B., and Märten, A., 1993, Geology and mineralogy of massive sulfide ores from the central Okinawa trough, Japan: ECONOMIC GEOLOGY, v. 88, p. 2210–2225.

Hitchman, S., Holland, I., and Evans, B., 2008, Technical report on Fosterville gold mine, Victoria, Australia: Unpublished report for Northgate Minerals, 122 p.

Honnorez, J., Honnorez-Guerstein, B., Vallete, J., and Wauschkuhn, A., 1976, Present day formation of an exhalative sulfide deposit at Vulcano (Thyrrhenian Sea), Part II: Active crystallization of fumarolic sulfides in the volcanic sediments of the Baja di Levante: International Union of Geological Sciences Series A, v. 3, p. 139–166.

Jessell, M.W., Willman, C.E., and Gray, D.R., 1994, Bedding parallel veins and their relationship to folding: Journal of Structural Geology, v. 16, p. 753–767.

Kraus, J., 2000, Back-rotation during crenulation cleavage development: Implications for structural facing and cleavage-forming processes (Discussion): Journal of Structural Geology, v. 22, p. 149–151.

Kuehn, C.A., and Rose, A.R., 1992, Geology and geochemistry of wall-rock alteration at the Carlin gold deposit, Nevada: ECONOMIC GEOLOGY, v. 87, p. 1697–1721.

Lamb, J.B., 1995, A petrographic and fluid inclusion study of the Purple Vein and Post/Betze orebodies, Carlin, Nevada: Unpublished M.Sc. thesis, University of Nevada.

Large, D.J., Sawłowicz, Z., and Spratt, J.A., 1999, Cobaltite-framboidal pyrite association from the Kupferschiefer: Possible implications for trace element behaviour during the earliest stages of diagenesis: Mineralogical Magazine, v. 63, p. 353–361.

Large, R.R., Maslennikov, V.V., Robert, F., Danyushevsky, L.V., and Chang, Z., 2007, Multi-stage sedimentary and metamorphic origin of pyrite and gold in the giant Sukhoi Log deposit, Lena gold province, Russia: ECONOMIC GEOLOGY, v. 102, p. 1233–1267.

Large, R.R., Danyushevsky, L., Hollit, C., Maslennikov, V., Meffre, S., Gilbert, S., Bull, S., Scott, R., Emsbo, P., Thomas, H., Singh, B., and Foster, J., 2009, Gold and trace element zonation in pyrite using a laser imaging technique: Implications for the timing of gold in orogenic and Carlin-style sediment-hosted deposits. ECONOMIC GEOLOGY, v. 104, p. 635–668.

Leader, L.D., Robinson, J.A., and Wilson, C.J.L., 2010, The role of faults and folding in controlling gold mineralisation at Fosterville, Victoria: Australian Journal of Earth Sciences, in press.

Li, X., Kwak, T.A. P., and Brown, R.W., 1998, Wallrock alteration in the Bendigo gold ore field, Victoria, Australia: Uses in exploration: Ore Geology Reviews, v. 13, p. 381–406.

Love, L.G., 1957, Microorganisms and the presence of syngenetic pyrite: Quarterly Journal of the Geological Society [London], v. 113, p. 429–440.

——1967, Early diagenetic iron sulphide in Recent sediments of The Wash, England: Sedimentology, v. 9, p. 327–352.

——1971, Early diagenetic polyframboidal pyrite, primary and redeposited, from the Wenlokian Denbigh Grit Group, Conway, North Wales, U.K.: Journal of Sedimentary Petrology, v. 41, p. 1038–1044.

Love, L.G., and Amstutz, G.C., 1966, Review of microscopic pyrite from the Devonian Chattanooga shale and Rammelsberg Banderz: Fortschritte der Mineralogie, v. 43, p. 273–308.

Love, L.G., and Zimmerman, D.O., 1961, Bedded pyrite and micro-organisms from the Mount Isa shale: ECONOMIC GEOLOGY, v. 56, p. 873–896.

Love, L.G., Al-Kaisy, A.T.H., and Brockley, H., 1984, Mineral and organic material in matrices and coatings of framboidal pyrite from Pennsylvanian sediments, England: Journal of Sedimentary Petrology, v. 54, 869–876.

Ludwig, K.R., 2003, User manual for Isoplot 3.0: Berkeley, California, Berkeley Geochronology Center Special Publication 4.

Meffre, S., Large, R., Scott, R., Chang, Z., Gilbert, S.E., Danyushevsky, L., Maslennikov V., Woodhead J., and Hergt J.M., 2008, Age and pyrite Pb-isotopic composition of the giant Sukhoi Log sediment-hosted gold deposit, Russia: Geochimica et Cosmochimica Acta, v. 72, p. 2377–2391.

Mernagh, T.P., 2001, A fluid inclusion study of the Fosterville mine: A turbidite-hosted gold field in the western Lachlan fold belt, Victoria, Australia: Chemical Geology, v. 173, p. 91–106.

Morse, J.W., and Cornwall, J.C., 1987, Analysis and distribution of iron sulfide minerals in recent anoxic marine sediments: Marine Chemistry, v. 22, p. 55–69.

Murowchick, J.B., 1992, Marcasite inversion and the petrographic determination of pyrite ancestry: ECONOMIC GEOLOGY, v. 87, p. 1141–1152.

Murowchick, J.B., and Barnes H.L., 1986, Marcasite precipitation from hydrothermal solutions: Geochimica et Cosmochimica Acta, v. 50, p. 2615–2629.

Pichler, T., Giggenbach, W.F., McInnes, B.I.A., Buhl, D., and Duck, B., 1999, Fe sulfide formation due to seawater-gas-sediment interaction in a shallow-water hydrothermal system at Lihir Island, Papua New Guinea: ECONOMIC GEOLOGY, v. 94, p. 281–288.

Pitcairn, I.K., Teagle, D.A.H., Craw, D., Olivo, G.R., Kerrich, R., and Brewer, T.S., 2006, Sources of metals and fluids in orogenic gold deposits: Insights from the Otago and Alpine schists, New Zealand: ECONOMIC GEOLOGY, v. 101, p. 1525–1546.

Offler, R., McKnight, S., and Morand, V., 1998, Tectonothermal history of the western Lachlan fold belt, Australia: Insights from white mica studies: Journal of Metamorphic Geology, v. 16, p. 531–540.

Ohfuji, H., and Rickard, D., 2005, Experimental synthesis of framboids—a review: Earth-Science Reviews, v. 71, p. 147–170.

Ohfuji, H., Boyle, A.P., Prior, D.J., and Rickard, D., 2005, Structure of framboidal pyrite: An electron backscatter diffraction study: American Mineralogist, v. 90, p. 1693–1704.

Ohfuji, H., Rickard, D., Light, M.E., and Hursthouse, M.B., 2006, Structure of framboidal pyrite: A single crystal X-ray diffraction study: European Journal of Mineralogy, v. 18, p. 93–98.

Raiswell, R., 1982, Pyrite texture, isotopic composition and the availability of iron: American Journal of Science, v. 282, p. 1244–1263.

Raiswell, R., and Berner, R.A., 1985, Pyrite formation in euxinic and semi-euxinic sediments: American Journal of Science, v. 285, p. 710–724.

Raiswell, R., and Canfield, D.E., 1998, Sources of iron for pyrite formation in marine sediments: American Journal of Science, v. 298, p. 219–245.

Raiswell, R., and Plant, J., 1980, The incorporation of trace elements into pyrite during diagenesis of black shales, Yorkshire, England: ECONOMIC GEOLOGY, v. 75, p. 684–699.

Raiswell, R., Whaler, K., Dean, S., Coleman, M.L., and Briggs, D.E.G., 1993, A simple three-dimensional model of diffusion-with-precipitation applied to localised pyrite formation in framboids, fossils and detrital iron minerals: Marine Geology, v.113, p. 89–100.

Raiswell, R., Newton, R., Bottrell, S.H ., Coburn, P.M., Briggs, D.E.G., Bond, D.P.G., and Poulton, S.W., 2008, Turbidite depositional influences on the diagenesis of Beecher's Trilobite Bed and the Hunsrück Slate: Sites of soft tissue pyritization: American Journal of Science, v. 308, p. 103–139.

Reedman, A.J., Colman, T.B., Campbell, S.D.G., and Howells, M.F., 1985, Volcanogenic mineralization related to the Snowdon Volcanic Group (Ordovician), Gwynedd, North Wales: Journal of the Geological Society [London], v. 142, p. 875–888.

Rickard, D.T., 1970, The origin of framboids: Lithos v. 3, p. 269–293.

——1975, Kinetics and mechanism of pyrite formation at low temperatures: American Journal of Science, v. 275, p. 636–652.

Rickard, D.T., and Zweifel, H., 1975, Genesis of Precambrian sulfide ores, Skellefte district, Sweden: ECONOMIC GEOLOGY, v. 70, p. 255–274.

Rust, G.W., 1935, Colloidal primary copper ores at Cornwall mines, southeastern Missouri: Journal of Geology, v. 43, p. 398–426.

Sassano, G.P., and Schrijver, K., 1989, Framboidal pyrite: Early-diagenetic, late-diagenetic, and hydrothermal occurrences from the Acton Vale quarry, Cambro-Ordovician, Quebec: American Journal of Science, v. 289, p. 167–179.

Sawłowicz, Z., 2000, Framboids: From their origin to application: Wroclaw-Warsaw, Poland, Polska Akademia Nauk, Komisja Nauk Mineralogicznych, Prace Mineralogiczne 88.

Schaubs, P.M., and Wilson, C.J.L., 2002, The relative roles of folding and faulting in controlling gold mineralization along the Deborah anticline, Bendigo, Victoria, Australia: ECONOMIC GEOLOGY, v. 97, p. 351–370.

Schneiderhöhn, H., 1923, Chalkographische Untersuchung des Mansfelde Kuperschiefers: Neues Jahrbuch fuer Mineralogie, Geologie und Paläeontologie, v. 47, p. 1–38.

Schouten, C., 1946, The role of sulphur bacteria in the formation of the so-called sedimentary copper ores and pyritic ore bodies: ECONOMIC GEOLOGY, v. 41, p. 517–538.

Skei, J.M., 1988, Formation of framboidal iron sulphide in the water of a permanently anoxic fiord, Framvaren, South Norway: Marine Chemistry v. 23, p. 345–352.

Stacey, J.S., and Kramers, J.D., 1975, Approximation of terrestrial lead isotope evolution by a two-stage model: Earth and Planetary Science Letters, v. 26, p. 207–221.

Stüwe, K., Keays, R.R., and Andrew, A., 1988, Wall rock alteration around gold quartz reefs at Wattle Gully mine, Ballarat slate belt, central Victoria [abs.]: Geological Society of Australia Abstracts Series 22, p. 478–480.

Sweeny, R.E., and Kaplan, I.R., 1973, Pyrite framboid formation: Laboratory synthesis and marine sediments: ECONOMIC GEOLOGY, v. 68, p. 618–634.

VandenBerg, A.H.M., Willman, C.E., Maher, S., Simons, B.A., Cayley, R.A., Taylor, D.H., Morand, V.J., Moore, D.H., and Radojkovic, A., 2000, The Tasman fold belt system in Victoria: Geological Survey of Victoria Special Publication, 462 p.

Wang, G.M., and White, S.H., 1993, Gold mineralisation in shear zones within a turbidite terrane, examples from Central Victoria, S. E. Australia: Ore Geology Reviews, v. 8, p. 163–188.

Wilkin, R.T., and Barnes, H.L., 1996, Pyrite formation by reactions of iron monosulfides with dissolved inorganic and organic sulfur species: Geochimica et Cosmochimica Acta, v. 60, p. 4167–4179.

——1997, Formation processes of framboidal pyrite: Geochimica et Cosmochimica Acta, v. 61, p. 323–339.

Wilkin, R.T., Barnes, H.L., and Brantley, S.L., 1996, The size distribution of framboidal pyrite in modern sediments: An indicator of redox conditions: Geochimica et Cosmochimica Acta, v. 60, p. 3897–3912.

Wilkin, R.T., Arthur, M.A., and Dean, W.E., 1997, The history of water-column anoxia in the Black Sea indicated by pyrite framboid size distributions: Earth and Planetary Science Letters, v. 148, p. 517–525.

Willman, C.E., 2007, Regional structural controls of gold mineralisation, Bendigo and Castlemaine goldfields, central Victoria, Australia: Mineralium Deposita, v. 42, p. 449–463.

Willman, C.E., and Wilkinson H.E., 1992, Bendigo goldfield, Spring Gully, Golden Square, Eaglehawk, 1:10,000 Maps geological report: Geological Survey of Victoria Report 93, 49 p.

Wilson, N.S.F., and Zentilli, M., 1999, The role of organic matter in the genesis of the El Soldado volcanic-hosted Manto-type Cu deposit, Chile: ECONOMIC GEOLOGY, v. 94, p. 1115–1135.

Wilson, N.S.F., Zentilli, M., and Spiro, B., 2003, A sulfur, carbon, oxygen, and strontium isotope study of the volcanic-hosted El Soldado Manto-type copper deposit, Chile: The essential role of bacteria and petroleum: ECONOMIC GEOLOGY, v. 98, p.163–174.

Woodhead, J.D., Hergt, J.M., Meffre, S., Large, R.R., Danyushevsky, L., and Gilbert, S., 2009, In situ Pb-isotope analysis of pyrite by laser ablation (multi-collector and quadrupole) ICPMS: Chemical Geology, v. 262, p. 344–354.

Zurkic, N., 1998, Fosterville gold deposits: Australasian Institute of Mining and Metallurgy Monograph Series 22, p. 507–510.

APPENDIX

Matrix Corrections to Framboidal Pyrite Pb Isotope Analyses

The relative proportions of shale matrix and pyrite in the ablated volumes was estimated from measured Al/Fe ratios for the quadrupole LA-ICPMS data as follows: Let Al_{matrix} and Fe_{matrix} be the Al and Fe contents (ppm), respectively, of pyrite-free matrix, and Fe_{py} (~465,000 ppm) be the Fe content of pyrite. If the proportion of matrix ablated in each analysis is X, and the measured Al/Fe ratio is y, then

$$y = \frac{X \times Al_{matrix}}{X \times Fe_{matrix} + (1-X) \times Fe_{py}}. \tag{1}$$

Rearranging equation 1 to solve for X yields:

$$X = \frac{y \times Fe_{py}}{Al_{matrix} + y\left(Fe_{py} - Fe_{matrix}\right)}. \tag{2}$$

Aluminum concentrations in whole-rock geochemical data for the sequence adjacent to sample SPD213_351.90 m were used to estimate Al_{matrix} and provide an internal standard with which to quantify LA-ICPMS analyses of relatively pyrite free matrix (Table 3). Once X is determined, the approximate proportions of Pb from pyrite and the matrix for each analysis were found as follows: the concentration of each of the four isotopes of Pb (${}^{n}Pb_{anal}$, where n denotes 204, 206, 207, or 208) is the sum of matrix and pyrite contributions, thus:

$${}^{n}Pb_{anal} = X \times {}^{n}Pb_{matrix} + \left(1 - X\right) \times {}^{n}Pb_{py}. \tag{3}$$

Rearranging equation 3 to solve for ${}^{n}\mathrm{Pb}_{py}$ yields:

$${}^{n}Pb_{py} = \frac{1}{\left(1-X\right)}\left[{}^{n}Pb_{anal} - X \times {}^{n}Pb_{matrix}\right]. \tag{4}$$

Because isotope concentrations (ppm) were determined assuming that Pb is almost entirely contained in pyrite (i.e., Fe_{py} used as internal standard) measured concentrations ${}^{n}Pb_{anal}$ do not represent the actual Pb concentration for the ablated volume, as required in equation 4. However, where Pb contributions from other sources (e.g., matrix) represent a small fraction of the total measured Pb (i.e., ${}^{n}Pb_{anal} \approx {}^{n}Pb_{py}$), the multiplication factor on the right side of equation 4 can be neglected, and a revised estimate of ${}^{n}Pb_{py}$, which approximately accounts for the matrix Pb component, is given by:

$${}^{n}Pb_{py} = {}^{n}Pb_{anal} - X \times {}^{n}Pb_{matrix}. \tag{5}$$

The total concentrations of each Pb isotope (i.e., ${}^{n}Pb_{anal}$ in eq. 5) in each analysis were determined using measured values of ${}^{206}\mathrm{Pb}/{}^{204}\mathrm{Pb}$, ${}^{207}\mathrm{Pb}/{}^{204}\mathrm{Pb}$, ${}^{208}\mathrm{Pb}/{}^{204}\mathrm{Pb}$ isotope ratios and total measured Pb concentration. Two different matrix compositions were used to model the likely matrix Pb contributions to framboidal pyrite analyses in sample RHD019_161.42 m (Table 4A-B). In Model 1 the Pb isotope composition of the matrix is based on data for sample SPD213_351.90 m (Fig. 17A, Table 3), and in Model 2 a more radiogenic composition based on LA-ICPMS data for a relatively pyrite free area in sample RHD019_161.42 m is used (Fig. 17B, Table

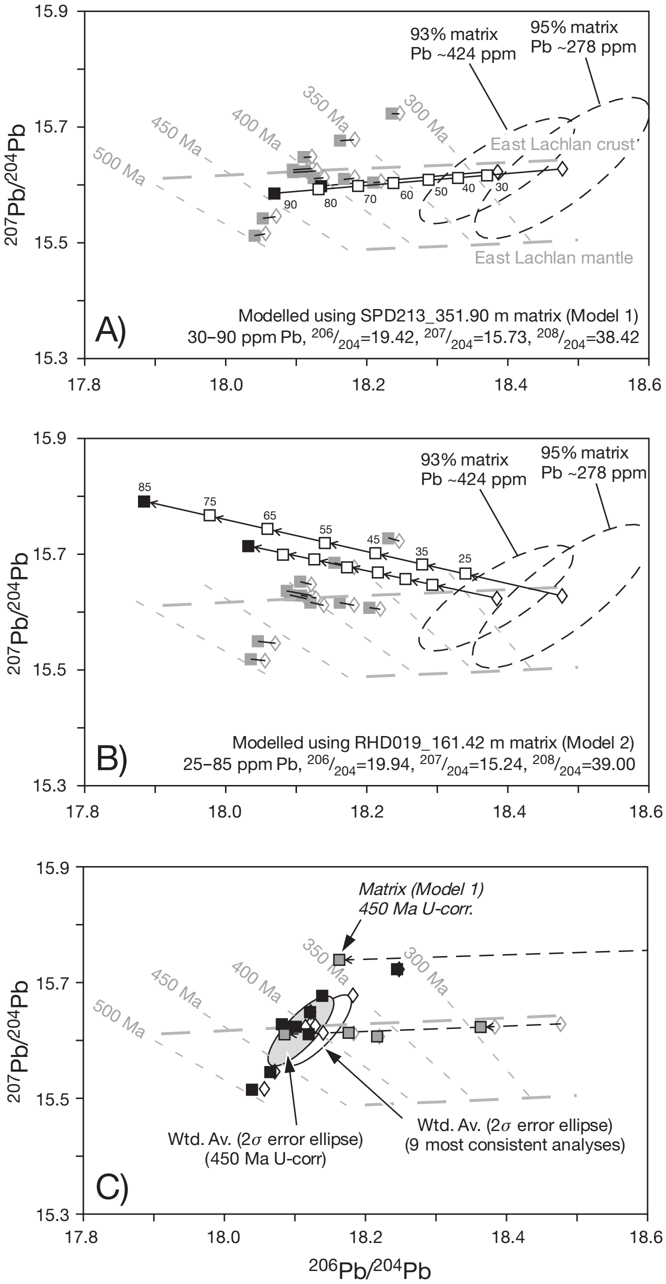

FIG. 17. ${}^{207}\mathrm{Pb}/{}^{204}\mathrm{Pb}$ vs. ${}^{206}\mathrm{Pb}/{}^{204}\mathrm{Pb}$ plots showing corrections to measured Pb isotope ratios for framboidal pyrite in sample RHD019_161.42 m (quadrupole LA ICPMS data) based on the estimated matrix (A) and (B) and U (C) contents of the ablation volumes. A. Model 1 (see Table 3). Open gray diamonds indicate measured isotopic ratios for ablation volumes containing >20 percent framboidal pyrite. Solid gray squares are corrected values assuming 90 ppm Pb in the matrix (matrix Pb isotope composition as indicated). Open black diamonds and 1σ error ellipses with dashed lines represent two analyses with <10 percent framboidal pyrite. Open squares show magnitude of correction for matrix Pb contents between 30 and 90 ppm Pb. B. Model 2 (see Table 3). As for (A) assuming more radiogenic matrix Pb. C. Maximum U corrections to pyrite Pb isotope data assuming a 450 Ma crystallization age. Open diamonds and filled squares denote measured and corrected Pb isotop ratios, respectively. Only data points in black were pooled to calculate weighted averages.

3). Results for both models indicate that for matrix Pb contents in the range 25 to 90 ppm Pb, the matrix only contributes significantly to measured Pb isotope ratios for ablation volumes containing <10 percent framboidal pyrite.

Corrections to the measured ^{206}Pb/^{204}Pb and ^{207}Pb/^{204}Pb ratios based on the estimated matrix proportion are similar to corrections accounting for the U contents of the ablated volumes (quadrupole ICPMS data only, Fig. 17C) based on the following formulas:

$$\left({}^{206}Pb/{}^{204}Pb\right)_{corr} = \left({}^{206}Pb/{}^{204}Pb\right)_{meas}\left[1-\left({}^{238}U/{}^{206}Pb\right)_{meas}\times\left(e^{k_1 t}-1\right)\right], \quad (6a)$$

$$\left({}^{207}Pb/{}^{204}Pb\right)_{corr} = \left({}^{207}Pb/{}^{204}Pb\right)_{meas}\left[1-\left({}^{238}U/{}^{206}Pb\right)_{meas}/137.9\times\left(e^{k_2 t}-1\right)\right], \quad (6b)$$

where k_1 (= 1.55125 × 10^{-10} y^{-1}) and k_2 (= 9.8485 × 10^{-10} y^{-1}) are the decay constants for ^{238}U and ^{235}U, respectively, t is the maximum crystallization age (y) and 137.9 is the ratio of ^{238}U/^{235}U.